ELSEVIER

Contents lists available at ScienceDirect

Journal of Computational Physics

journal homepage: www.elsevier.com/locate/jcp



The hybrid-dimensional Darcy's law: a non-conforming reinterpreted discrete fracture model (RDFM) for single-phase flow in fractured media



Ziyao Xu^a, Zhaoqin Huang^b, Yang Yang^{c,*}

- ^a Division of Applied Mathematics, Brown University, Providence, RI 02906, United States of America
- ^b School of Petroleum Engineering, China University of Petroleum, Qingdao, Shangdong, China
- ^c Department of Mathematical Sciences, Michigan Technological University, Houghton, MI 49931, United States of America

ARTICLE INFO

Article history: Received 28 January 2021 Received in revised form 16 October 2022

Accepted 30 October 2022 Available online 8 November 2022

Keywords:

Hybrid-dimensional Darcy's law Fracture and barrier networks Non-conforming meshes Local discontinuous Garlerkin methods

ABSTRACT

In this paper, we propose a novel discrete fracture model for flow simulation of fractured porous media containing flow blocking barriers on non-conforming meshes. The methodology of the approach is to modify the traditional Darcy's law into the hybrid-dimensional Darcy's law where fractures and barriers are represented as Dirac-δ functions contained in the permeability tensor and resistance tensor, respectively. As a natural extension of the previous discrete fracture model [21] for highly conductive fractures, this model is able to account for the influence of both highly conductive fractures and blocking barriers accurately on non-conforming meshes. The local discontinuous Galerkin (LDG) method is employed to accommodate the form of the hybrid-dimensional Darcy's law and the nature of the pressure/flux discontinuity. The performance of the model is demonstrated by several numerical tests.

© 2022 Elsevier Inc. All rights reserved.

1. Introduction

Fractures are ubiquitous in crustal rocks as a result of geological process such as jointing and faulting, which have a substantial impact on the hydraulic properties of the rock mass. Fractures can serve as high-conductivity conduits or barriers for fluid and solute transport depending on whether fractures are filled with impermeable minerals or not [2,1, 16]. Understanding and modeling fluid flow in fractured media is of great importance in various engineering applications, such as oil and gas exploitation, CO₂ sequestration, geothermal extraction, and radioactive waste disposal. As an efficient approach, discrete fracture models (DFM) are usually used in the flow modeling of fractured media, in which the fractures are represented individually. To accurately capture the complexity of a fractured media, unstructured grids are commonly required to explicitly discretize the complex fracture geometries in DFM. Based on DFM, a series of corresponding numerical methods, including FVM [4,8,27–29], FEM [10,9,30], mixed FEM [14,5,39,31–34], and mimetic finite difference method [6] have been applied to the flow simulations in fractured media. However, great difficulties can be brought into the mesh

E-mail addresses: ziyao_xu1@brown.edu (Z. Xu), huangzhqin@upc.edu.cn (Z. Huang), yyang7@mtu.edu (Y. Yang).

^{*} The second author was funded by the National Nature Science Foundation of China 52074336, the Major Science and Technology Projects of China National Petroleum Corporation ZD2019-183-008. The last author was funded by the NSF grant DMS-1818467 and Simons Foundation 961585.

^{*} Corresponding author.

generation processes when the complex fracture geometries are highly developed. The use of conforming grids in real geological models is still limited due to the complex gridding and high computational cost.

As a compromise, the embedded discrete fracture model (EDFM), a kind of nonconforming mesh method, is proposed [11, 12]. In this approach, the structured grids are usually used to discretize the reservoir domain, and the fractures are directly incorporated into the background grids. Fracture grids are generated by segmenting fractures with the structured background grids, and additional non-neighboring connections and transmissivities are introduced to explicitly consider the influence of fractures. The EDFM has been widely applied to reservoir containing highly-conductive fractures, and implemented in various complex problems. Moinfar et al. [15] implemented the EDFM in an in-house compositional reservoir simulator for nonvertical fractures. Panfili et al. [18] and Fumagalli et al. [3] applied the EDFM to perform case studies with corner-point grids. Xu and Sepehrnoori [20] gave the detailed algorithms and workflow for the implementation of EDFM in corner-point grids. Liu et al. [13] proposed a modified EDFM to improve the fracture discretization process by using two sets of independent grids for matrix and fracture systems, which promotes the modeling of 3D complex fracture geometries in real-field geological structures. However, the conventional EDFM is not suitable in cases when fractures behave as barriers, i.e. the fracture permeability lies far below that of the matrix. To resolve this limitation, the projection-based EDFM (pEDFM) is proposed [19,7]. The effective flow area between adjacent matrix grids is calculated using the original interface area minus the projected area of the fracture segment, which will become zero if the fracture fully penetrates through the matrix cell. Olorode et al. [17] extended the pEDFM into three-dimensional compositional simulation of fractured reservoirs.

In this paper, we extend the idea in DFM, which accounts for the influence of fractures by superposing the stiffness matrices (FEM-DFM) or fluxes (FVM-DFM) contributed by fractures on that of porous matrix, to model barriers in a similar fashion. Recall that in the classical FEM-DFM, the fractures are aligned with edges of meshes in order to superpose the stiffness matrices of fractures on that of porous matrix conveniently. We have revealed [21] that such an approach is equivalent to employing the FEM on the same mesh to the modified Darcy's law, in which the permeability tensor of fractures represented by Dirac- δ functions are superposed on the permeability tensor of porous matrix. It's not difficult to see that the equivalence also holds for FVM-DFM if we apply FVM on the same mesh to the modified Darcy's law. The approach of adding barriers in the model is drawn from the simple observation that the Darcy's law in one space dimension can be written as $k^{-1}u = -\frac{dp}{dx}$, in which k^{-1} can be explained as the resistance as in the Ohm's law. The barriers thus can be viewed as the region with high resistance, in contrast with the high permeability region of fractures. Therefore, we can also represent the barriers by Dirac- δ functions in a similar way as we did in modeling fractures and the only issue remains is to quantify the blocking ability of barriers. Though the idea of the model inherits from DFM, its implementation is more similar to the pEDFM, in the sense that it can be naturally applied on structured meshes, in particular on rectangular meshes, since the model is built on the partial differential equations level thereby independent of meshes. However, unlike the pEDFM, which modifies the way of handling conductive fractures from the original EDFM, our approach adds the ability to model low permeability barriers while preserves the original way of modeling conductive fractures in our previous work.

The rest of the paper is organized as follows. In section 2, we model barriers in 1D porous media. In section 3, we extend the model to two space dimensions and fracture barrier networks. In section 4, we establish the numerical scheme of the novel discrete fracture model based on local discontinuous Galerkin method. The performance of the approach for steady-state single-phase flow in 2D porous media is demonstrated by several well-known benchmarks in section 5. Finally, we show an application of the model in contaminant transportation in porous media in section 6.

2. Modeling barriers in 1D porous media

To rationalize the formulation of the hybrid-dimensional Darcy's law, this section explores the hybrid-dimensional model for barriers in 1D porous media.

2.1. Equi-dimensional model for barriers in 1D porous media

For the steady-state single-phase flow in 1D porous media, the Darcy's velocity u and pressure p are governed by the following differential equations,

$$u = -k(x)\frac{dp}{dx}, \quad x \in (a, b), \tag{2.1}$$

$$\frac{du}{dx} = f, \quad x \in (a, b), \tag{2.2}$$

where k(x) is the permeability of the porous media and f is the source term. The equation (2.1) is known as the Darcy's law. When the porous media contains low permeable barrier regions, the permeability k(x) can be expressed as follows,

$$k(x) = \begin{cases} k_m & x \in \Omega_m \\ k_{\epsilon} & x \in \Omega_{\epsilon}, \end{cases}$$
 (2.3)

where k_m is the permeability of porous matrix, k_ϵ is the permeability of barrier, Ω_m and Ω_ϵ denote the matrix region and barrier region, respectively. See Fig. 1(a) for an illustration, in which the barrier region $\Omega_\epsilon = (x_1 - \frac{\epsilon}{2}, x_1 + \frac{\epsilon}{2})$ is colored black

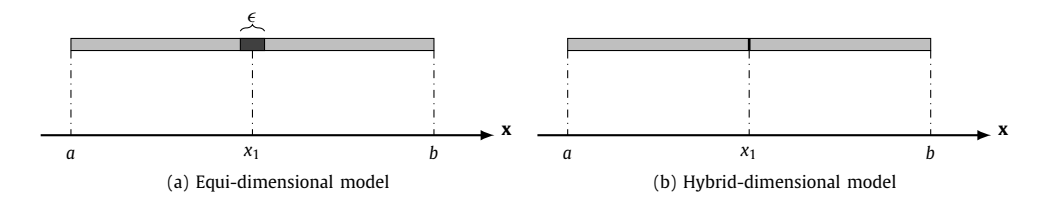


Fig. 1. Barrier model in 1D porous media.

gray and the matrix region $\Omega_m = (a, b) \setminus \Omega_{\epsilon}$ is colored light gray. Note that the thickness of barrier region is exaggerated for the sake of visibility here.

We consider the Dirichlet boundary conditions for this problem, i.e.

$$p(a) = p_a, \quad p(b) = p_b.$$
 (2.4)

The equations (2.1), (2.2) and (2.4) are called the equi-dimensional model for barriers in 1D porous media.

2.2. Hybrid-dimensional model for barriers in 1D porous media

Following the idea in our previous work [21], which uses Dirac- δ functions to describe highly conductive fractures, this section explores the hybrid-dimensional representation for barriers in 1D porous media.

If there is no source term, the Darcy's velocity u can be solved from the equations (2.1), (2.2) and (2.4):

$$u = \frac{p_a - p_b}{\int_a^b \frac{dx}{k(x)}}.$$
(2.5)

In analogy to the Ohm's law RI = U, we can rewrite equation (2.5) as

$$\left(\int_{a}^{b} \frac{dx}{k(x)}\right) u = p_a - p_b,$$

where $\int_{a}^{b} \frac{dx}{k(x)}$ can be interpreted as the resistance of the porous media.

Replace b by the variable $x \in (a, b)$, the resistance of porous media on interval (a, x) can be approximated as $\int_{x}^{x} \frac{dx}{k(x)} \approx$

$$\int\limits_{-\infty}^{x} \frac{dx}{k_m} + \frac{\epsilon}{k_\epsilon} H(x-x_1), \text{ where } H(x) \text{ is the Heaviside function defined as } H(x) = 1 \text{ when } x \ge 0 \text{ while } H(x) = 0 \text{ when } x < 0.$$

Therefore the following governing equation of integration form holds:

$$\left(\int_{a}^{x} \frac{dx}{k_{m}} + \frac{\epsilon}{k_{\epsilon}} H(x - x_{1})\right) u = p_{a} - p(x), \quad x \in (a, b).$$

The corresponding differentiation form is the hybrid-dimensional barrier model, which can be viewed as a modified version of Darcy's law:

$$\left(k_m^{-1} + \frac{\epsilon}{k_{\epsilon}}\delta(x - x_1)\right)u = -\frac{dp}{dx}, \quad x \in (a, b),$$
(2.6)

where δ is the Dirac- δ function. If there are multiple barriers in the media, the equation becomes

$$\left(k_m^{-1} + \sum_{i=1}^M \frac{\epsilon_i}{k_{\epsilon_i}} \delta(x - x_i)\right) u = -\frac{dp}{dx}, \quad x \in (a, b)$$
(2.7)

where M is the number of barriers and x_i 's are the positions of barrier's centers.

Equations (2.7), (2.2) and (2.4) are called the hybrid-dimensional model for barriers in 1D porous media.

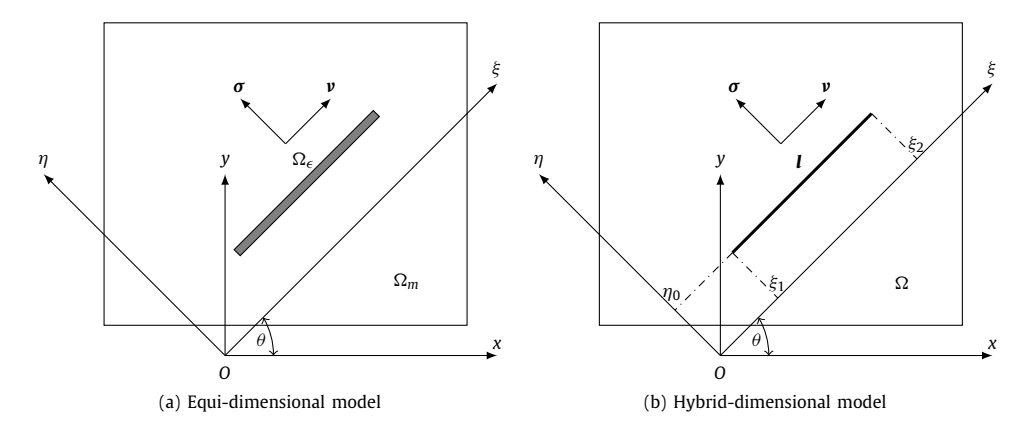


Fig. 2. Barrier model in 2D porous media.

3. Hybrid-dimensional Darcy's law for 2D porous media

This section extends the hybrid-dimensional model for barriers from 1D to 2D and then presents the complete formulation of the hybrid-dimensional Darcy's law by combining it with the fracture model [21].

3.1. Hybrid-dimensional model for barriers in 2D porous media

For the steady-state single-phase flow in 2D porous media, the Darcy's velocity u and pressure p are governed by the following partial differential equations,

$$\mathbf{K}^{-1}\mathbf{u} = -\nabla p, \quad x \in \Omega \tag{3.1}$$

$$\nabla \cdot \mathbf{u} = f, \quad \mathbf{x} \in \Omega \tag{3.2}$$

where $\mathbf{K}(\mathbf{K}^{-1})$ is the permeability (resistance) tensor of the porous media.

We consider the mixed boundary condition

$$p = p_D$$
, on $\Gamma_D \in \partial \Omega$, and $\boldsymbol{u} \cdot \boldsymbol{n} = q_N$, on $\Gamma_N = \partial \Omega \setminus \Gamma_D$, (3.3)

where \boldsymbol{n} is the unit outer normal vector of the boundary $\partial \Omega$.

When the porous media contains low permeable barrier strips, see Fig. 2(a), the permeability K can be expressed as follows,

$$\mathbf{K} = \begin{cases} \mathbf{K}_m & x \in \Omega_m \\ \mathbf{K}_{\epsilon} & x \in \Omega_{\epsilon}, \end{cases}$$
 (3.4)

where Ω_m is the matrix region and Ω_{ϵ} is the barrier region, and \mathbf{K}_m and \mathbf{K}_{ϵ} are the permeability tensors of these two regions, respectively.

Analogous to (2.6) and note that the effect of a barrier on the flow in its tangential direction v is negligible, we propose the hybrid-dimensional barrier model for 2D porous media:

$$\left(\mathbf{K}_{m}^{-1} + \frac{\epsilon}{k_{\epsilon}} \delta(\cdot) \mathbb{1}(\cdot) \boldsymbol{\sigma} \boldsymbol{\sigma}^{T}\right) \boldsymbol{u} = -\nabla p, \tag{3.5}$$

where ϵ is the thickness of the barrier, k_{ϵ} is the permeability of the barrier in its normal direction, σ is the unit normal vector of the barrier \mathbf{I} , $\delta(\cdot)$ and $\mathbb{1}(\cdot)$ are the shorthand of two functions containing the information of the position of the barrier \mathbf{I} .

The full expressions of $\delta(\cdot)$ and $\mathbb{1}(\cdot)$ under the local coordinate system $\xi O \eta$ and global coordinate system xOy are given as

$$\delta(\cdot) = \delta(\eta - \eta_0) = \delta(-\sin(\theta)x + \cos(\theta)y - \eta_0),\tag{3.6}$$

and

$$\mathbb{1}(\cdot) = \mathbb{1}(\xi_1 \le \xi \le \xi_2) = \mathbb{1}(\xi_1 \le \cos(\theta)x + \sin(\theta)y \le \xi_2),\tag{3.7}$$

where δ is the Dirac- δ function and $\mathbb 1$ is the indicator function defined as $\mathbb 1$ (expr) equals 1 if expr is true while equals 0 otherwise. For the coordinate systems $\xi O \eta$ and xO y, see Fig. 2 as an illustration.

3.2. Hybrid-dimensional Darcy's law for fracture and barrier networks in 2D porous media

In the previous work [21], we proposed the hybrid-dimensional fracture model in 2D porous media:

$$\mathbf{u} = -\left(\mathbf{K}_m + \epsilon k_f \delta(\cdot) \mathbb{1}(\cdot) \mathbf{v} \mathbf{v}^T\right) \nabla p, \tag{3.8}$$

where ϵ is the thickness of the fracture, k_f is the permeability of the fracture in its tangential direction, ν is the unit tangential vector of the fracture, and $\delta(\cdot)$, $\mathbb{1}(\cdot)$ are the shorthand of their full expressions as in (3.6) and (3.7) that contain the geometric information of the fracture.

Combining the barrier model (3.5) and fracture model (3.8) together, we obtain the hybrid-dimensional Darcy's law for single-phase flow in fractured media containing fracture and barrier networks:

$$\left(\mathbf{I} + \mathbf{K}_{m} \sum_{i=1}^{M} \frac{\epsilon_{i}}{k_{\epsilon_{i}}} \delta_{i}(\cdot) \mathbb{1}_{i}(\cdot) \boldsymbol{\sigma}_{i} \boldsymbol{\sigma}_{i}^{T}\right) \boldsymbol{u} = -\left(\mathbf{K}_{m} + \sum_{i=M+1}^{M+N} \epsilon_{i} k_{f_{i}} \delta_{i}(\cdot) \mathbb{1}_{i}(\cdot) \boldsymbol{v}_{i} \boldsymbol{v}_{i}^{T}\right) \nabla p,$$

$$(3.9)$$

where i = 1, ..., M are barriers and i = M + 1, ..., M + N are fractures.

Note that in 3D model, we can follow [21] and replace $v_i v_i^T$ by $I - \sigma_i \sigma_i^T$ on the right hand side of (3.9).

Remark 3.1. In (3.9), the conductive fractures and blocking barriers appear on two different sides of the equation. Considering the huge variation of fracture permeability in reservoirs, the proper identification of fractures and barriers in a fracture network is crucial. In practice, we adopt a simple criteria to identify their types. If the fracture permeability is greater than the matrix permeability, i.e. $k_f > k_m$, we identify it as a conductive fracture and put its parameters on the right hand side of the equation (3.9), otherwise we identify it as a blocking barrier and put its parameters on the left hand side of (3.9).

We also would like to note that, if $k_f \approx k_m$ or $k_\epsilon \approx k_m$, the impact of the conductive fracture or blocking barrier on the flow is negligible as $\epsilon k_f \approx \epsilon k_m \approx 0$ and $\frac{\epsilon}{k_\epsilon} \approx \frac{\epsilon}{k_m} \approx 0$, since $\epsilon \approx 0$ compared with the scale of porous matrix.

4. Numerical algorithm of the novel discrete fracture model

In this section, we establish the numerical algorithm of the novel discrete fracture model (3.9), (3.2) and (3.3) by applying the local discontinuous Galerkin (LDG) method to it, see [35,36] for more details of the method. For brevity, we only consider the 2D case.

4.1. Basic notations

For the computational domain Ω , consider the partition \mathcal{T} , i.e. $\Omega = \bigcup_{T \in \mathcal{T}} T$, where T's are elements in the partition. We denote $\Gamma = \bigcup_{T \in \mathcal{T}} \{e | e \in \partial T\}$ to be the collection of cell interfaces and $\Gamma_0 = \Gamma \setminus \partial \Omega$ for all interior ones.

For a scalar-valued function v, define its jump and average on $e = \partial T_1 \cap \partial T_2 \in \Gamma_0$ by

$$[v]_e = v_1 \mathbf{n}_1 + v_2 \mathbf{n}_2, \qquad \{v\}_e = \frac{1}{2}(v_1 + v_2),$$

where $v_i = v|_{T_i}$ and \textbf{n}_i is the unit outer normal vector of edge ∂T_i in T_i . For convenience, if $e \in \partial \Omega$, we denote $[v]_e = v \textbf{n}$ and $\{v\}_e = v$, where n is the unit outer normal of $\partial \Omega$. Similarly, the jump and average of a vector-valued function w are defined as

$$[\mathbf{w}]_e = \mathbf{w}_1 \cdot \mathbf{n}_1 + \mathbf{w}_2 \cdot \mathbf{n}_2, \quad \{\mathbf{w}\}_e = \frac{1}{2}(\mathbf{w}_1 + \mathbf{w}_2),$$

for $e = \partial T_1 \cap \partial T_2 \in \Gamma_0$, and $[\boldsymbol{w}]_e = \boldsymbol{w} \cdot \boldsymbol{n}$, $\{\boldsymbol{w}\}_e = \boldsymbol{w}$ for $e \in \partial \Omega$.

Moreover, define the broken inner product for scalar-valued functions as

$$(u, v) = \sum_{T \in \mathcal{T}} \int_{T} uv \, dx dy,$$

and for vector-valued functions as

$$(\boldsymbol{u}, \boldsymbol{v}) = \sum_{T \in \mathcal{T}} \int_{T} \boldsymbol{u} \cdot \boldsymbol{v} \, dx dy.$$

4.2. LDG scheme

We take the finite element spaces as

$$V_h = \{ v \in L^2(\Omega) : v|_T \in P^k(T), \forall T \in T \} \text{ and } \boldsymbol{W}_h = V_h \times V_h,$$

where $P^k(T)$ denotes the space of polynomials of degree at most k on triangular element T, or

$$V_h = \{v \in L^2(\Omega) : v|_T \in Q^k(T), \forall T \in T\} \text{ and } \boldsymbol{W}_h = V_h \times V_h,$$

where $Q^k(T)$ denotes the space of tensor products of 1D polynomials of degree at most k on rectangular element T.

Lemma 4.1 will help us reduce the 2D integration of the line Dirac- δ terms in (3.9) to line integrals on fractures and barriers. One can find the detailed proof in [21].

Lemma 4.1. Let $\delta(\cdot)$ and $\mathbb{1}(\cdot)$ be the shorthand of their full expressions in (3.6) and (3.7), respectively. For all continuous function g on Ω , the following identity holds:

$$\int_{\Omega} \delta(\cdot) \mathbb{1}(\cdot) g(x, y) \, dx dy = \int_{\Omega} g(x, y) \, ds, \tag{4.1}$$

where **l** is the support of $\delta(\cdot) \mathbb{1}(\cdot)$ as shown in Fig. 2(b).

Now we introduce the auxiliary variable $\mathbf{s} = -\nabla p$ and establish the LDG scheme for the model problem (3.9), (3.2) and (3.3) as follows:

Find $\mathbf{s}, \mathbf{u} \in \mathbf{W}_h$ and $p \in V_h$, such that $\forall \mathbf{\xi}, \mathbf{\eta} \in \mathbf{W}_h, \zeta \in V_h$,

$$(\mathbf{s}, \boldsymbol{\xi}) = (p, \nabla \cdot \boldsymbol{\xi}) - \int_{\Gamma_0 \cup \Gamma_N} \hat{p}[\boldsymbol{\xi}] ds - \int_{\Gamma_D} p_D \boldsymbol{\xi} ds, \tag{4.2}$$

$$(\boldsymbol{u}, \boldsymbol{\eta}) + \sum_{i=1}^{M} \int_{\boldsymbol{l}_{i}} \left(\frac{\epsilon_{i}}{k_{\epsilon_{i}}} \mathbf{K}_{\mathbf{m}} \boldsymbol{\sigma}_{i} \boldsymbol{\sigma}_{i}^{T} \boldsymbol{u} \right) \cdot \boldsymbol{\eta} \, ds = (\mathbf{K}_{m} \boldsymbol{s}, \boldsymbol{\eta}) + \sum_{i=M+1}^{M+N} \int_{\boldsymbol{l}_{i}} \left(\epsilon_{i} k_{f_{i}} \boldsymbol{v}_{i} \boldsymbol{v}_{i}^{T} \boldsymbol{s} \right) \cdot \boldsymbol{\eta} \, ds, \tag{4.3}$$

$$-(\boldsymbol{u}, \nabla \zeta) + \int_{\Gamma_0 \cup \Gamma_0} \hat{\boldsymbol{u}} \cdot [\zeta] \, ds + \int_{\Gamma_N} q_N \zeta \, ds = (f, \zeta), \tag{4.4}$$

where $\hat{\boldsymbol{u}}$ and \hat{p} are numerical fluxes defined by

$$\hat{\boldsymbol{u}}|_{e} = \begin{cases} \{\boldsymbol{u}\}, & \text{if } T_{1} \cup T_{2} \text{ is crossed by some barriers } \boldsymbol{l}_{i}, i = 1, 2, \cdots, M \\ \{\boldsymbol{u}\} + \alpha[p], & \text{otherwise.} \end{cases}$$
(4.5)

$$\hat{p}|_{e} = \begin{cases} \{p\} + \beta[\mathbf{u}], & \text{if } T_{1} \cup T_{2} \text{ is crossed by some barriers } \mathbf{l}_{i}, i = 1, 2, \cdots, M \\ \{p\}, & \text{otherwise}, \end{cases}$$

$$(4.6)$$

on $e = \partial T_1 \cap \partial T_2 \in \Gamma_0$, and $\hat{\boldsymbol{u}}|_e = \boldsymbol{u} + \alpha \, (p - p_D) \, \boldsymbol{n}$ on $e = \partial T \cap \Gamma_D$, and $\hat{p}|_e = p$ on $e = \partial T \cap \Gamma_N$, where $\alpha, \beta > 0$ are penalty parameters, and \boldsymbol{n} is the unit outer normal vector of $\partial \Omega$.

Remark 4.1. It turns out to be crucial to take the correct penalty on the jump of \boldsymbol{u} and p for a successful simulation when defining the numerical fluxes. The reason why we enforce the penalty in this way is, physically, the normal component of the Darcy's velocity \boldsymbol{u} is continuous across a barrier but might be discontinuous across a fracture, while the pressure p is discontinuous when crossing a barrier but is continuous in all other cases. In the special case where some barriers happen to be aligned (or very close to be aligned) with some cell interfaces, we can take a subtle adaptation on the penalties in the numerical fluxes (4.5) and (4.6) to improve the accuracy of the simulation, by enforcing the penalty on jump of \boldsymbol{u} only on the aligned edges and enforcing the penalty on jump of p on other edges of that cell if no other barrier crosses it.

Remark 4.2. Unlike other models that generate system of equations only for pressure p, the LDG methods gives system of equations for the unknown pressure p, Darcy's velocity u and the pressure gradient s. This difference makes our methods to be computationally more costly than other methods since the degrees of freedom increases a lot. However, it's not a total disadvantage since in many applications what really useful is the Darcy's velocity and gradient of pressure rather than the pressure itself, and by computing these variables simultaneously, the accuracy of Darcy's velocity and gradient of pressure is higher than those obtained from the post processing of pressure.

Two issues in implementation are worthy to be mentioned. First, as one may notice, if the fracture or barrier I happens to be aligned with cell interfaces of a mesh, the ambiguity of the line integral on I in scheme (4.3) needs to be resolved. Rigorously speaking, we should use a well-defined trace of u or s in (4.3) on the cell interfaces to replace of the double-valued u or s, e.g. $\operatorname{tr}(u)|_{I} = \{u\}$, $\operatorname{tr}(s)|_{I} = \{s\}$, which is equivalent to divide the fracture or barrier I equally into its two neighboring cells. However, in practice, we can take the advantage of the non-conforming nature of our algorithm to add very tiny random perturbations on the position of I and only code for the non-conforming case, which is what we shall do in the numerical experiments in the following section. Second, to treat the special case where fractures and barriers have intersections, say I_1 and I_2 intersect on the cell I, we only consider either $I_1 \cap I$ or $I_2 \cap I$ on I, and remove the other one, depending on whether the fracture I_1 penetrates the barrier I_2 (fracture-dominated) or the barrier I_2 blocks the fracture I_1 (barrier-dominated), which is determined by geologists based on the desire of application.

4.3. Slope limiter

Due to the discontinuity of pressure across barriers and numerical features of LDG, the numerical approximation of pressure may have strong oscillations on cells containing barriers. Therefore, a properly designed slope limiter to eliminate spurious oscillations on those cells is essential in the post-processing of numerical approximation of pressure.

One such limiter was introduced in [37] and modified in [38,39]. The key idea of the limiter is to achieve an appropriate maximum-principle of pressure on barrier cells by imposing the constraint that the value of pressure on a vertex o lies between the minimum and the maximum of the cell averages of neighboring cells of this vertex while make the change as small as possible.

Since we only apply the slope limiter on cells containing barriers rather than on all cells, we adapt the limiter in [38,39] in a way that might be less accurate but is easier to implement. The slope limiting of p on a target cell T with vertices o_1, o_2, \ldots, o_n (n = 4 for rectangular meshes) is shown as follows:

$$\tilde{p}_T(x) = \bar{p}_T + \theta \left(p_T(x) - \bar{p}_T \right), \tag{4.7}$$

where $\bar{p}_T = \frac{1}{|T|} \int_T p_T(x) dx$ is the cell average, and $\theta \in [0,1]$ is chosen to be the largest possible value such that $\tilde{p}_T(o_i) \in [p_i^{\min}, p_i^{\max}]$, for $i = 1, \dots, n$, where $p_i^{\min} = \min_{o_i \in K} \{\bar{p}_K\}$ and $p_i^{\max} = \max_{o_i \in K} \{\bar{p}_K\}$. It's clear from (4.7) that this limiter doesn't change the cell average.

The calculation of θ in (4.7) can be explicitly given as follows:

$$\theta = \min_{i=1,2,...,n} \theta_{i}, \quad \text{where } \theta_{i} = \begin{cases} \min\{\frac{p_{i}^{\min} - \bar{p}_{T}}{p_{T}(o_{i}) - \bar{p}_{T}}, 1\}, & \text{if } p_{T}(o_{i}) < \bar{p}_{T}, \\ 1 & \text{if } p_{T}(o_{i}) = \bar{p}_{T}, \\ \min\{\frac{p_{i}^{\max} - \bar{p}_{T}}{p_{T}(o_{i}) - \bar{p}_{T}}, 1\}, & \text{if } p_{T}(o_{i}) > \bar{p}_{T}. \end{cases}$$

$$(4.8)$$

For the original slope limiter, which is of course applicable in our algorithm, one can refer to the appendix of [39], where an intuitive graphical explanation is given.

On cells where the penalty on jump of p is imposed on some edges, the pressure oscillation is greatly depressed by the scheme itself, thereby we don't need to apply the slope limiter on them. These include the cells that are not crossed by any barrier, and the cells whose only partial edges are aligned with barriers as is discussed in Remark 4.1.

5. Numerical experiments

In this section, we provide four numerical experiments, in an order of increasing geometric complexity, to demonstrate the performance of the reinterpreted discrete fracture model (RDFM) proposed in the paper. The implementations use the piecewise linear finite element spaces, i.e. k=1 in V_h , unless otherwise stated. The Example 5.3 and 5.4 are benchmarks taken from [22–26], so one can refer to the solutions in these articles for reference. For simplicity, the flow in all examples is driven by boundary conditions thus the source term f=0 in (3.2).

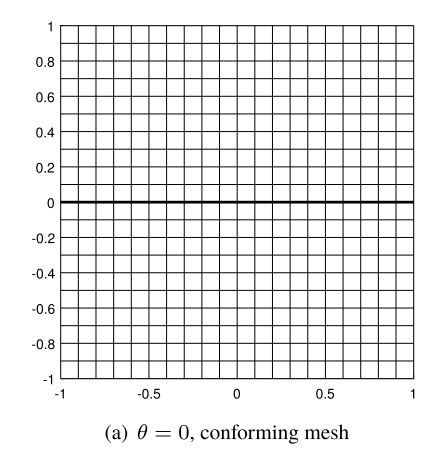
Flemisch et al. [22] published the data of grids and solutions of several benchmarks computed by a number of DFM algorithms on [40], which enables us to evaluate and compare our model with the existing ones. We declare that all the data and figures used in Example 5.3 and 5.4 for references, evaluations and comparison come from them.

We made the data and source codes of our example available on https://github.com/ziyaoxu/HybridDarcy. One can also find data, figures and source codes of more numerical tests on the website, which include the benchmarks in [22–24].

Example 5.1. Convergence test

In this example, we test the convergence of our algorithm. We provide the analytical solutions of two particular cases, which are the single fracture case and the single barrier case described in case (a) and case (b), respectively. In both cases, the domain is set to be $\Omega = [-1, 1] \times [-1, 1]$ and the permeability of the matrix $\mathbf{K}_m = \mathbf{I}$.

Case (a): Single-fracture Consider the fluid flow in the porous media containing a single fracture across the domain. Suppose the fracture passes the origin with its tangential direction $\mathbf{v} = (\cos(\theta), \sin(\theta))^T$, the thickness $\epsilon = 10^{-4}$, and the tangential permeability $k_f = 2 \times 10^4$, then the corresponding governing equation is



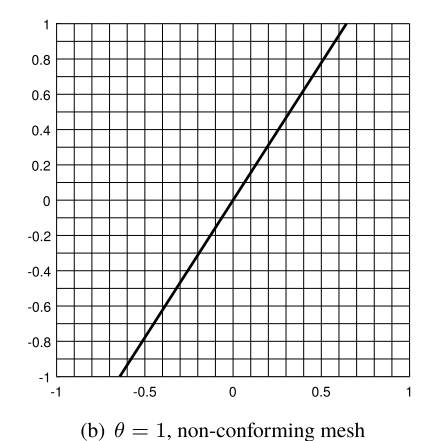


Fig. 3. The single fracture/barrier with different angles in Example 5.1.

Table 1 Error table of Example 5.1 with order k = 1.

	Case (a)				Case (b)				
	$\theta = 0$		$\theta = 1$		$\theta = 0$		$\theta = 1$		
$N \times N$	L ¹ error	order							
20 × 20	1.82e-03	-	1.26e-02	-	1.89e-04	-	6.10e-02	-	
40×40	4.58e-04	1.99	9.02e-03	0.48	4.73e-05	2.00	3.08e-02	0.98	
80×80	1.14e-04	2.00	4.35e-03	1.05	1.18e-05	2.00	1.54e-02	1.00	
160×160	2.85e-05	2.00	2.64e-03	0.72	2.96e-06	2.00	8.39e-03	0.88	
320×320	7.10e-06	2.00	1.41e-03	0.91	7.39e-07	2.00	3.72e-03	1.18	
$N \times N$	L ² error	order							
20 × 20	1.34e-03	_	9.74e-03	_	1.23e-04	_	1.47e-01	_	
40×40	3.39e-04	1.98	7.32e-03	0.41	3.07e-05	2.00	1.08e-01	0.44	
80×80	8.47e-05	2.00	3.49e-03	1.07	7.68e-06	2.00	7.60e-02	0.51	
160×160	2.11e-05	2.01	2.10e-03	0.73	1.92e-06	2.00	5.38e-02	0.50	
320×320	5.26e-06	2.00	1.12e-03	0.91	4.80e-07	2.00	3.83e-02	0.49	

$$\mathbf{u} = -\left(\mathbf{I} + 2\delta(-\sin(\theta)x + \cos(\theta)y) \begin{bmatrix} \cos^2(\theta) & \sin(\theta)\cos(\theta) \\ \sin(\theta)\cos(\theta) & \sin^2(\theta) \end{bmatrix}\right) \nabla p, \quad \nabla \cdot \mathbf{u} = 0$$

One can verify that $p(x, y) = \sin(\cos(\theta)x + \sin(\theta)y)e^{|-\sin(\theta)x + \cos(\theta)y|}$ is the analytical solution of the equation under the corresponding Dirichlet boundary conditions.

Case (b): Single-barrier Consider the fluid flow in the porous media containing a single barrier across the domain. Suppose the barrier passes the origin with its tangential direction $\mathbf{v} = (\cos(\theta), \sin(\theta))^T$, the thickness $\epsilon = 10^{-4}$, and the normal permeability $k_{\epsilon} = 10^{-4}$, then the corresponding governing equation is

$$\left(\mathbf{I} + \delta(-\sin(\theta)x + \cos(\theta)y) \begin{bmatrix} \sin^2(\theta) & -\sin(\theta)\cos(\theta) \\ -\sin(\theta)\cos(\theta) & \cos^2(\theta) \end{bmatrix}\right) \mathbf{u} = -\nabla p, \quad \nabla \cdot \mathbf{u} = 0$$

The exact solution is $p(x, y) = (\sin(\theta) - \cos(\theta))x - (\sin(\theta) + \cos(\theta))y + H(\sin(\theta)x - \cos(\theta)y)$, where H(x) is the Heaviside function, under the corresponding Dirichlet boundary conditions.

By taking different θ , we can test the errors and rates of convergence in both conforming and non-conforming scenarios, see Fig. 3. The error tables with the order of finite element spaces k=1 and k=2 are given in Table 1 and Table 2, respectively.

A brief summery is given as follows.

For tests of case(a), the rates of convergence are optimal when meshes are aligned with the fracture (as aforementioned, the meshes are not rigorously conforming but almost conforming up to a tiny perturbation on the position of the fracture for convenience of coding, so this condition is not so strong.) Further tests show that the rates of convergence remain optimal on conforming meshes for higher order k's, under the setting of penalty parameter $\alpha = O(1/h^{k+1})$. As for the non-conforming meshes, the rate of convergence remains first order for k > 1, due to the low regularity of the exact solution

¹ Due to the restriction of the memory of the computer, we are unable to compute the solution on 320×320 mesh for k = 2.

Table	2						
Error	table	of	Example	5.1	with	order	k=2.

	Case (a)				Case (b)				
	$\theta = 0$		$\theta = 1$	$\theta = 1$		$\theta = 0$			
$N \times N$	L ¹ error	order	L ¹ error	order	L ¹ error	order	L ¹ error	order	
20 × 20	1.04e-04	-	2.12e-03	-	1.89e-05	-	5.73e-02	-	
40×40	1.31e-05	2.98	5.95e-04	1.83	2.37e-06	3.00	3.12e-02	0.88	
80×80	1.65e-06	3.00	2.46e-04	1.27	2.96e-07	3.00	1.52e-02	1.04	
160×160	2.06e-07	3.00	1.32e-04	0.90	3.69e-08	3.00	8.44e-03	0.85	
$N \times N$	L ² error	order	L ² error	order	L ² error	order	L ² error	order	
20 × 20	7.94e-05	_	2.30e-03	_	1.23e-05	_	1.41e-01	_	
40×40	9.71e-06	3.03	8.88e-04	1.37	1.54e-06	3.00	1.08e-01	0.39	
80×80	1.20e-06	3.02	3.18e-04	1.48	1.92e-07	3.00	7.40e-02	0.54	
160×160	1.48e-07	3.01	1.74e-04	0.87	2.40e-08	3.00	5.45e-02	0.44	

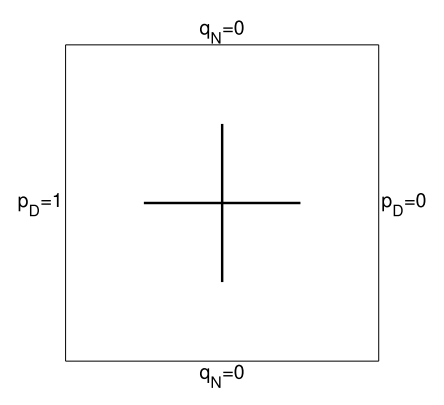


Fig. 4. Domain and boundary conditions of Example 5.2.

 $(p \in H^1(\Omega))$. But the errors are still reduced significantly when k increases. It's notable that we found $\alpha = O(1/h^3)$ is needed for the algorithm to be convergent for $k \ge 1$ on non-conforming meshes.

For tests of case(b), the rates of convergence are optimal when meshes are aligned with the barrier. Further tests show that the rates of convergence remain optimal on conforming meshes for higher order k's, under the setting of penalty parameter $\alpha = O(1/h)$, $\beta = O(1/h^{k+1})$. As for the non-conforming meshes, the rate of convergence remains first order in L^1 norm and half order in L^2 norm for $k \ge 1$, due to the low regularity of the exact solution $(p \in H^s(\Omega), s < \frac{1}{2})$. And the errors are almost unchanged when k increases. It's notable that we found setting $\alpha = O(1/h)$, $\beta = O(1/h)$ is sufficient for the algorithm to be convergent for k > 1 on non-conforming meshes.

To this end, we would like to note that, the reference solutions in this example actually show the ability of our model to handle the mass transfer between matrix and fractures. We give a detailed demonstration in the Appendix C.

Example 5.2. Cross-shaped networks

In this example, we test the cross-shaped fracture network and barrier network in case (a) and case (b), respectively. In both cases, the domain is the unit square $\Omega = [0,1] \times [0,1]$ with permeability of porous matrix $\mathbf{K}_m = \mathbf{I}$. The region of fractures/barriers is $[0.25,0.75] \times [0.4995,0.5005] \cup [0.4995,0.5005] \times [0.25,0.75]$, see Fig. 4. Moreover, the Dirichlet boundary conditions $p_D = 1$ and $p_D = 0$ are imposed on the left and right boundaries respectively, and the top and bottom boundaries are set to be impermeable, i.e. $q_N = 0$. This example is the same with the test case given by [19], so one can refer to the solution of it for a comparison.

Case (a): Cross-shaped fractures The permeability of fractures is $k_f = 10^8$.

Case (b): Cross-shaped barriers The permeability of barriers is $k_{\epsilon} = 10^{-8}$.

The reference solutions are computed by finite element method on the 1001×1001 fully resolved mesh and plotted in Fig. 5. The solutions of RDFM on different meshes for case (a) and case (b) are shown in Fig. 6 and Fig. 7, respectively.

Comparing the numerical solutions of RDFM with the reference solutions, we can see the effect of conductive fractures and blocking barriers are captured well on coarse meshes. Moreover, the pressure along the fracture paralleling to the flow direction on the 11×11 mesh of case (a) is flat. This phenomenon is reasonable since the domain, mesh and boundary conditions are symmetric.

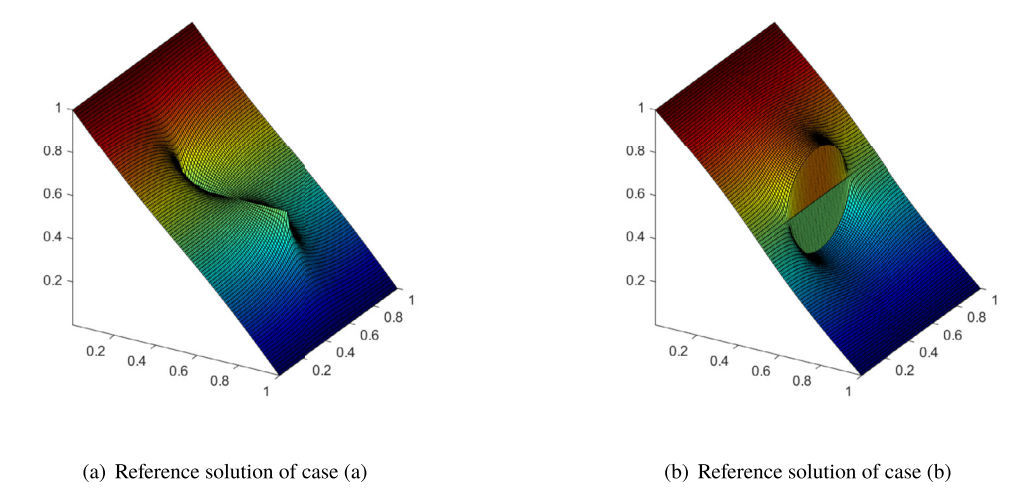


Fig. 5. The reference solutions of Example 5.2.

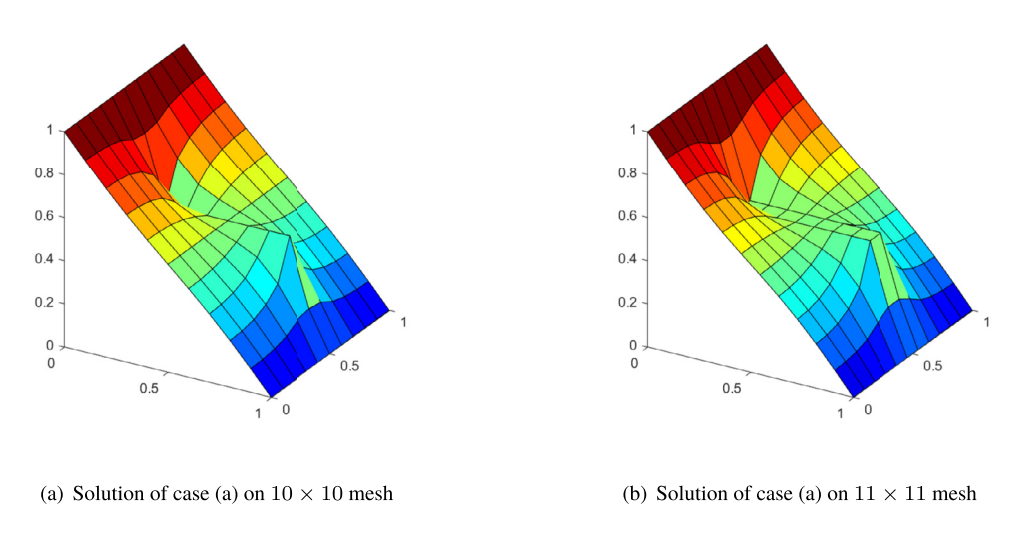


Fig. 6. Simulation results of case (a) of Example 5.2.

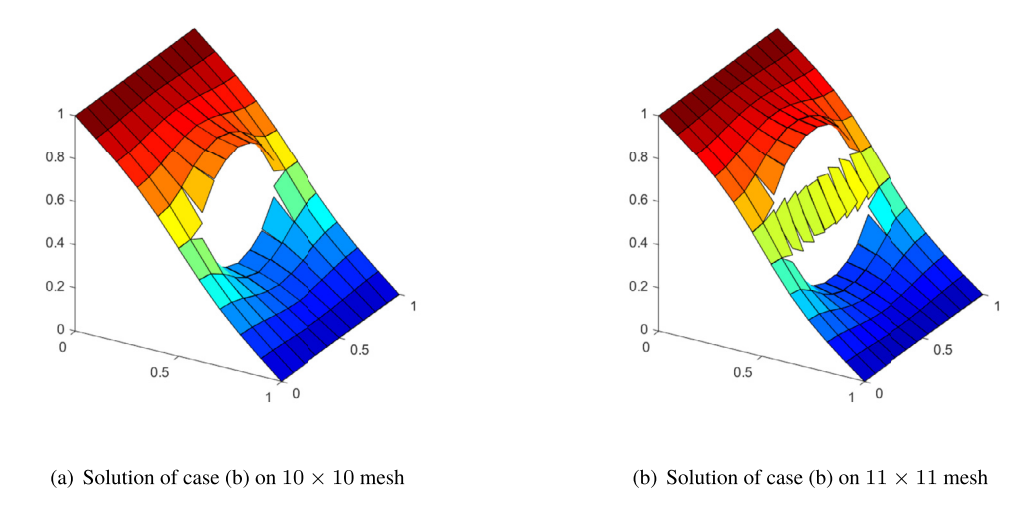


Fig. 7. Simulation results of case (b) of Example 5.2.

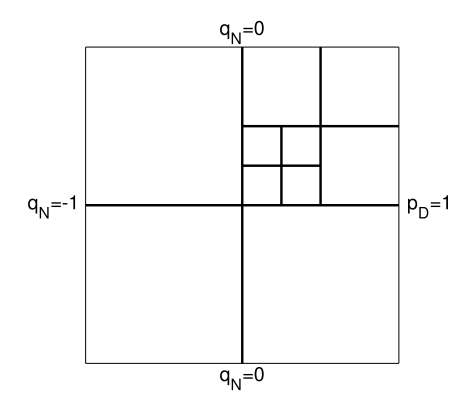


Fig. 8. Domain and boundary conditions of Example 5.3.

Table 3Evaluation data of different methods of case (a) of Example 5.3.

method	matrix elements	fracture elements	d.o.f.	mesh	err _m	err_f
Box-DFM	2691 triangles	130	1422	conforming	6.7e-03	1.1e-03
CC-DFM	1386 triangles	95	1481	conforming	1.1e-02	5.0e-03
EDFM	1369 rectangles	132	1501	non-conforming	6.5e-03	4.0e-03
Mortar-DFM	1280 triangles	75	3366	conforming	1.0e-02	7.4e-03
P-XFEM	961 rectangles	318	1632	non-conforming	1.7e-02	6.0e-03
D-XFEM	1250 triangles	126	4474	non-conforming	9.6e-03	8.9e-03
RDFM	625 rectangles	90	12500	non-conforming	8.6e-03	8.8e-03
RDFM	1225 rectangles	126	24500	non-conforming	5.9e-03	6.2e-03

Example 5.3. Regular networks

In this example, we test regular networks of fractures and barriers. This example was originally from [24] and modified by [22], which contains two subcases. The case (a) is a fracture network and the case (b) is a barrier network. In both cases, the domain is the unit square $\Omega = [0, 1] \times [0, 1]$ with permeability $\mathbf{K}_m = \mathbf{I}$. The networks are composed of six fractures/barriers with central axis x = 0.5, y = 0.5, x = 0.75, y = 0.75, x = 0.625, y = 0.625 and uniform thickness $\epsilon = 10^{-4}$, see Fig. 8. The left boundary is imposed by Neumann boundary condition $q_N = -1$ and the right boundary is imposed by Dirichlet boundary condition $p_D = 1$. The top and bottom boundaries are impermeable.

Case (a): Regular fracture network The permeability of fractures is $k_f = 10^4$. **Case (b): Regular barrier network** The permeability of barriers is $k_{\epsilon} = 10^{-4}$.

The reference solutions are provided by [22] based on the mimetic finite difference (MFD) method on a very fine mesh containing 1136456 matrix elements and 38600 fracture elements. The methods participate in the comparison are the vertex-centered control volume discrete fracture model (Box-DFM), the cell-centered two point flux approximation control volume discrete fracture model (CC-DFM), the embedded discrete fracture model (EDFM), the mortar-flux discrete fracture model (Mortar-DFM), the primal extended finite element method (P-XFEM), and the dual extended finite element method (D-XFEM), refer to [22] for a detailed introduction.

We first test our model on non-conforming meshes. To demonstrate its performance comprehensively, we conduct the computation on two rectangular meshes with different grid sizes. The coarse mesh is 25×25 while the fine mesh is 35×35 . We plot the contours of pressure for both cases in Fig. 9. One can find the contours of reference solutions in [22] for comparison. We also slice the profiles of the pressure along the line y = 0.7 and x = 0.5 for case (a) and the line (0.0, 0.1) - (0.9, 1.0) for case (b), and draw the comparison with the reference solutions and other models in Fig. 10 and Fig. 11, respectively.

Furthermore, we compute the model on 8×8 and 16×16 uniform rectangular meshes. Note that the meshes are conforming in this case. We plot the contours of pressure for both cases in Fig. 12. The slices of the solutions along the line y = 0.7 and x = 0.5 for case (a) and the line (0.0, 0.1) - (0.9, 1.0) for case (b) are shown in Fig. 13 and Fig. 14 respectively, together with those of reference solutions. We don't draw slices of other methods again since they are already shown in the previous comparisons.

A quantitative comparison of relative errors, together with other important aspects of different models, are summarized in the Table 3 and Table 4 for case (a) and case (b), respectively, in which d.o.f. is the shorthand of the degrees of freedom. The relative errors on matrix and fractures/barriers of a solution are defined as:

$$\operatorname{err}_{\mathbf{m}}^{2} = \frac{1}{|\Omega|(\Delta p_{\text{ref}})^{2}} \sum_{i,j} |T_{\text{ref}}^{i} \cap T_{\mathbf{m}}^{j}| \left(p_{\text{ref}}|_{T_{\text{ref}}^{i}} - p_{\mathbf{m}}|_{T_{\mathbf{m}}^{j}} \right)^{2}, \tag{5.1}$$

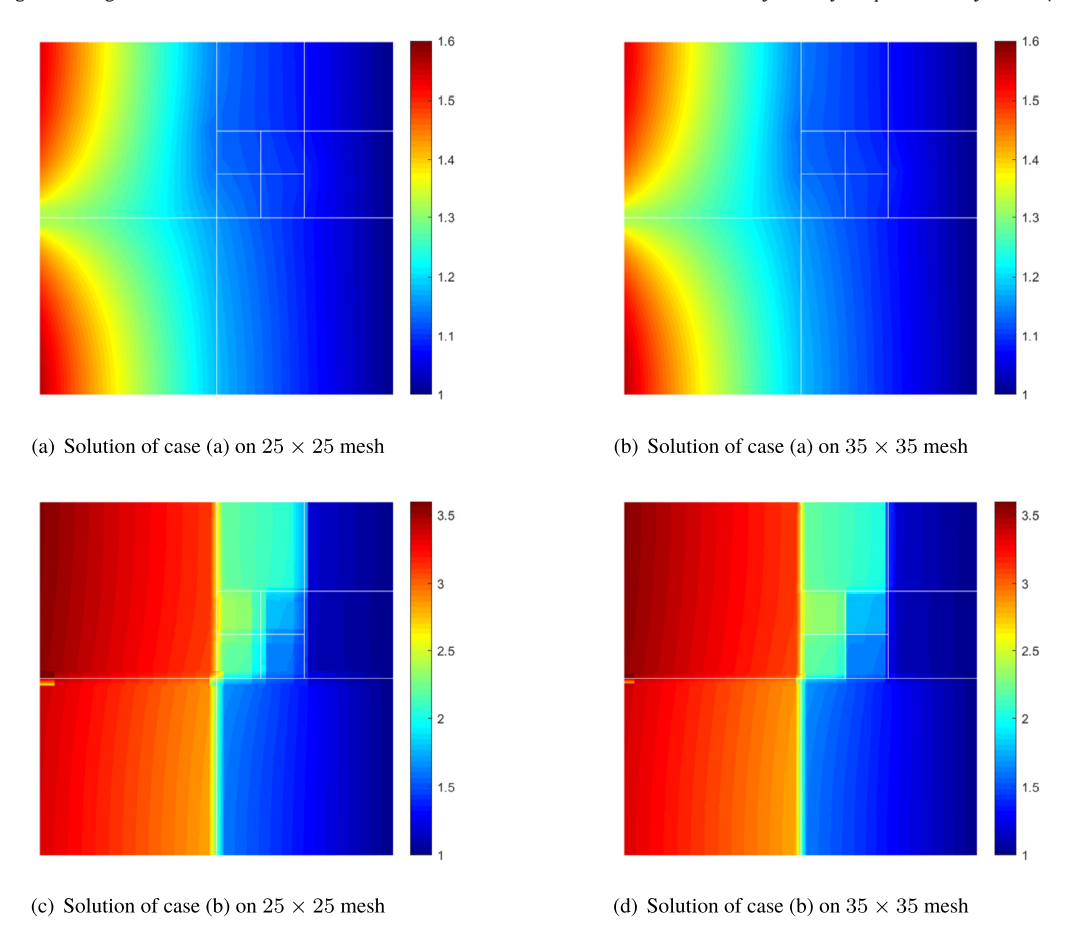


Fig. 9. Simulation results of Example 5.3 on non-conforming meshes. (For interpretation of the colors in the figure(s), the reader is referred to the web version of this article.)

Table 4 Evaluation data of different methods of case (b) of Example 5.3.

method	matrix elements	fracture elements	d.o.f.	mesh	err _m	err_f
Box-DFM	2691 triangles	130	1422	conforming	4.1e-01	3.8e-01
CC-DFM	1386 triangles	95	1481	conforming	5.7e-03	4.6e-03
EDFM	1369 rectangles	132	1501	non-conforming	2.9e-01	3.2e-01
Mortar-DFM	1280 triangles	75	3366	conforming	4.5e-03	4.9e-03
P-XFEM	961 rectangles	318	1632	non-conforming	2.9e-03	2.2e-02
D-XFEM	1250 triangles	126	4474	non-conforming	1.0e-02	1.9e-02
RDFM	625 rectangles	90	12500	non-conforming	3.1e-02	4.0e-02
RDFM	1225 rectangles	126	24500	non-conforming	2.6e-02	4.2e-02

$$\operatorname{err}_{f}^{2} = \frac{1}{|\Gamma|(\Delta p_{\operatorname{ref}})^{2}} \sum_{i,l} |T_{\operatorname{ref}}^{i} \cap T_{f}^{l}| \left(p_{\operatorname{ref}}|_{T_{\operatorname{ref}}^{i}} - p_{f}|_{T_{f}^{l}} \right)^{2}, \tag{5.2}$$

where $|\Omega|$ and $|\Gamma|$ are measures of the matrix and fractures respectively, $p_{\rm ref}$ is the reference solution, $\Delta p_{\rm ref} = \max p_{\rm ref} - \min p_{\rm ref}$ is the range of the reference solution, $T_{\rm ref}^i$, $i=1,2,\ldots,I$, are cells employed for the reference solution, $T_{\rm m}^i$, $j=1,2,\ldots,J$, and $T_{\rm f}^l$, $l=1,2,\ldots,L$, are the matrix elements and fracture elements employed for the method to be evaluated, respectively, see [22] for more details about the definition.

We want to point out that, due to the discontinuity of pressure across barriers, the relative error on barriers is not a good indicator of accuracy. This concept even doesn't make much sense in our model since we use delta function to represent the barrier. That's why the relative error of pressure on barriers fails to converge in our method, but this doesn't mean the model is failed. In fact, as one can see from the slices of solutions along (0.0, 0.1) - (0.9, 1.0) and the relative errors on the porous matrix, our method provides good approximations in barriers network case, especially on the conforming meshes.

In Appendix D, we take a cursory investigation on the high order method for this problem on a sparse conforming triangulation.

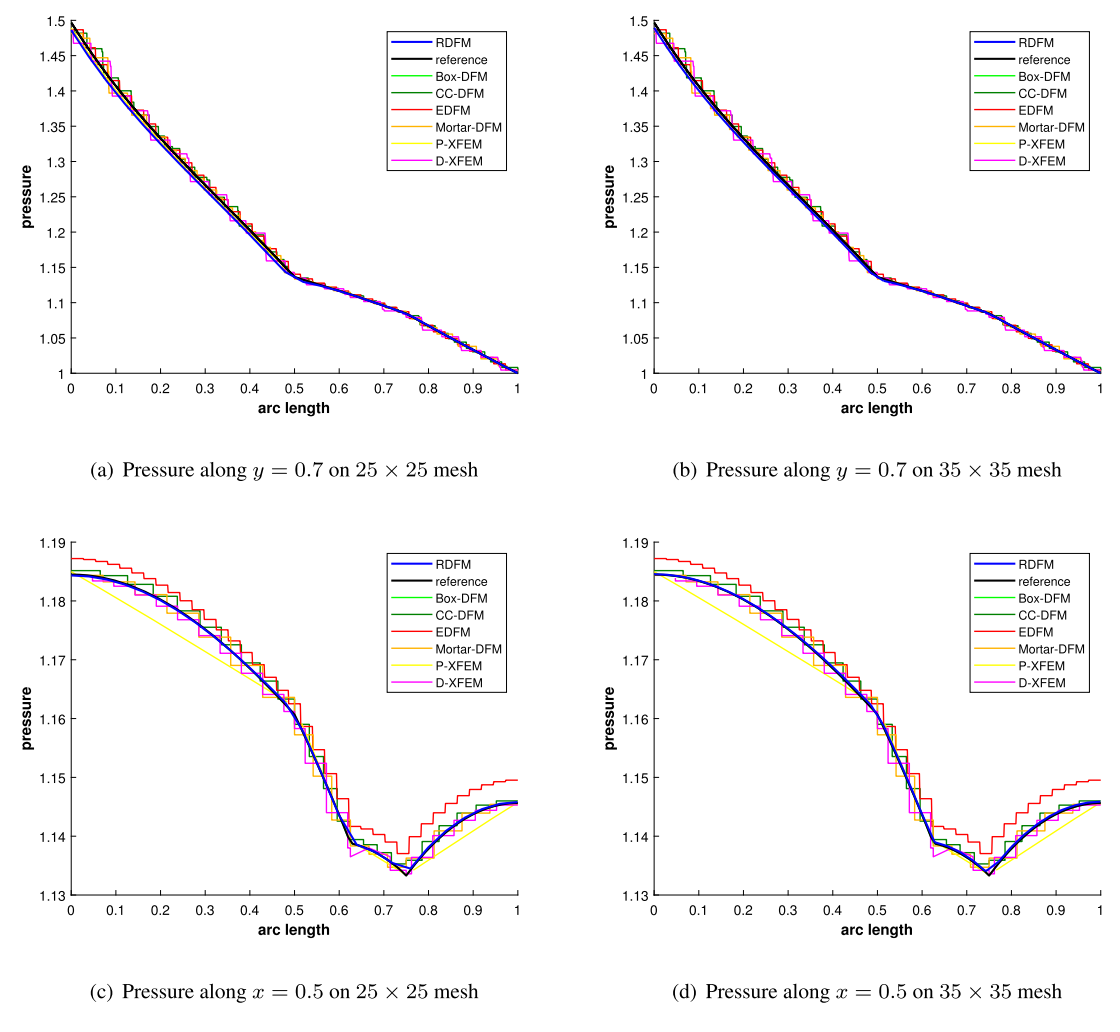


Fig. 10. Slices of pressure in case (a) of Example 5.3 on non-conforming meshes.

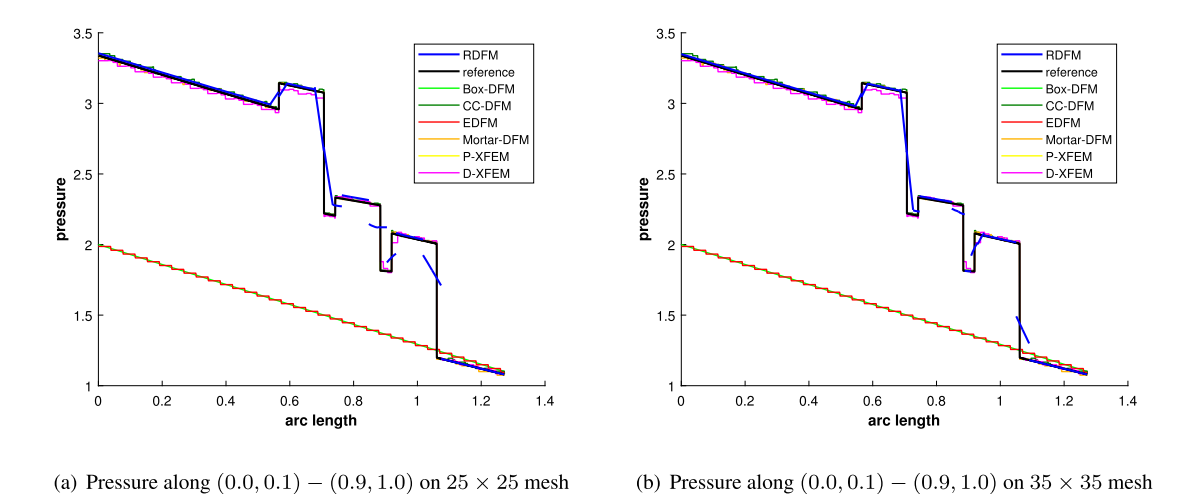


Fig. 11. Slices of pressure in case (b) of Example 5.3 on non-conforming meshes.

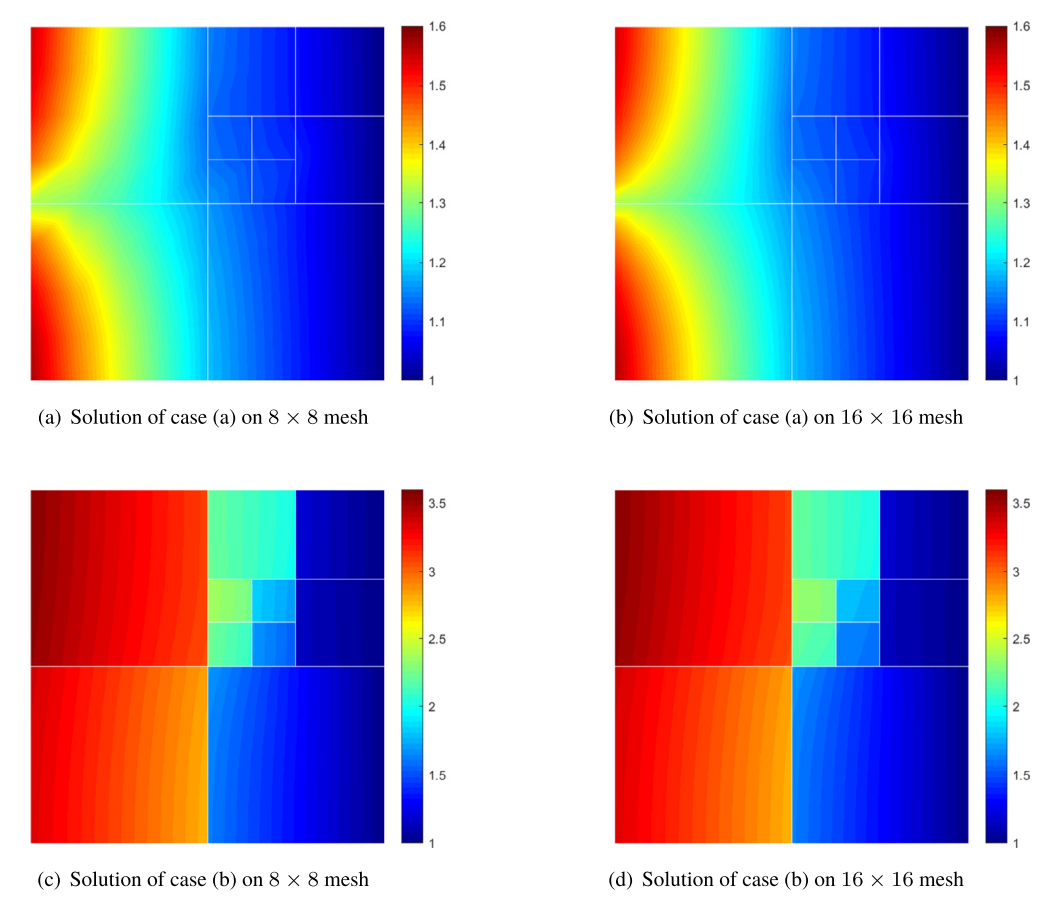


Fig. 12. Simulation results of Example 5.3 on conforming meshes.

Table 5Evaluation data of different methods of case (a) of Example 5.4.

method	matrix elements	fracture elements	d.o.f.	mesh	err_m	err_f
Box-DFM	2838 triangles	155	1460	conforming	4.4e-02	3.8e-02
CC-DFM	1407 triangles	103	1510	conforming	2.6e-02	3.3e-02
EDFM	1369 rectangles	203	1572	non-conforming	3.8e-02	4.5e-02
Mortar-DFM	1452 triangles	105	3953	conforming	1.0e-02	1.7e-02
D-XFEM	1922 triangles	199	7180	non-conforming	1.9e-02	2.9e-02
RDFM	900 rectangles	167	18000	non-conforming	2.4e-02	3.5e-02
RDFM	1600 rectangles	219	32000	non-conforming	1.8e-02	3.1e-02

Example 5.4. Complex networks

In this example, we test complex networks containing 8 fractures and 2 barriers. This example is taken from the benchmark 4.3 in [22]. The distribution of fractures and barriers are shown in Fig. 15, in which fractures are colored red and barriers are colored blue. The computational domain is the unit square $\Omega = [0, 1] \times [0, 1]$ with permeability $\mathbf{K}_m = \mathbf{I}$. The exact coordinates of the fractures and barriers are attached in the appendix A. All fractures and barriers have the uniform thickness 10^{-4} with permeability $k_f = 10^4$ and $k_\epsilon = 10^{-4}$, respectively.

Case (a): Flow from top to bottom The top and bottom boundaries are Dirichlet with $p_D = 4$ and $p_D = 1$ respectively. The left and right boundaries are impermeable.

Case (b): Flow from left to right The left and right boundaries are Dirichlet with $p_D = 4$ and $p_D = 1$ respectively. The top and bottom boundaries are impermeable.

The reference solutions are computed by MFD on a very fine mesh containing 1192504 matrix elements and 7876 fracture elements. The models that participate in the comparison are the same as before excepts the P-XFEM, which could not join due to its severe restriction on the geometry of fracture networks. Moreover, another version of cell centered control volume discrete fracture model (CC-DFM*) without the elimination of intermediate fracture intersection cells is included in the comparison for case (b).

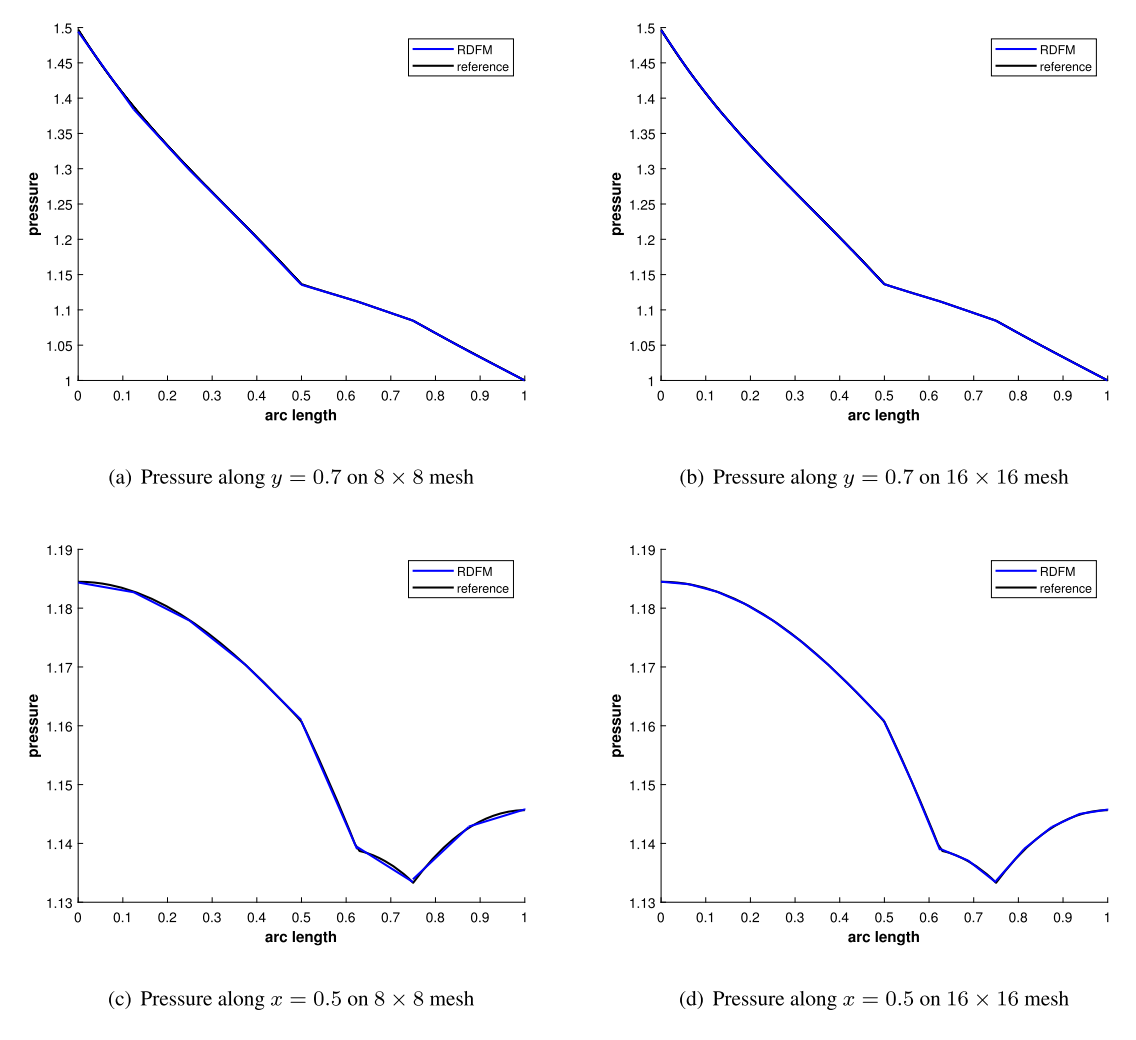


Fig. 13. Slices of pressure in case (a) of Example 5.3 on conforming meshes.

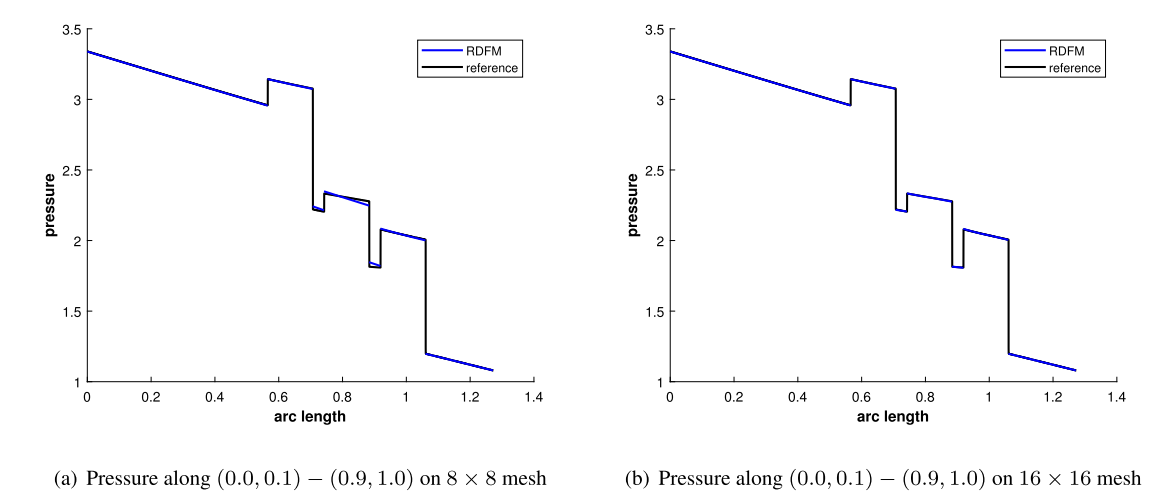


Fig. 14. Slices of pressure in case (b) of Example 5.3 on conforming meshes.

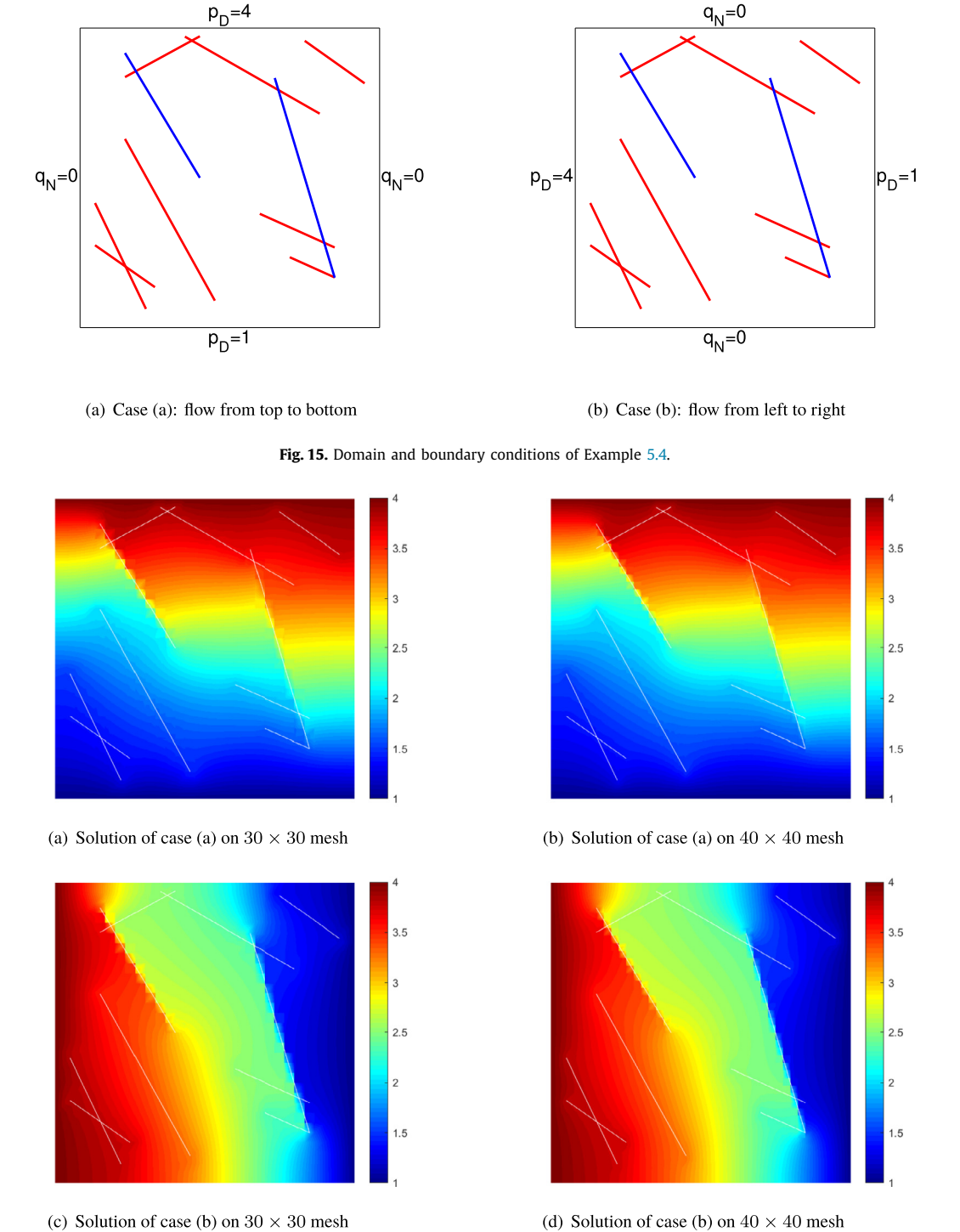
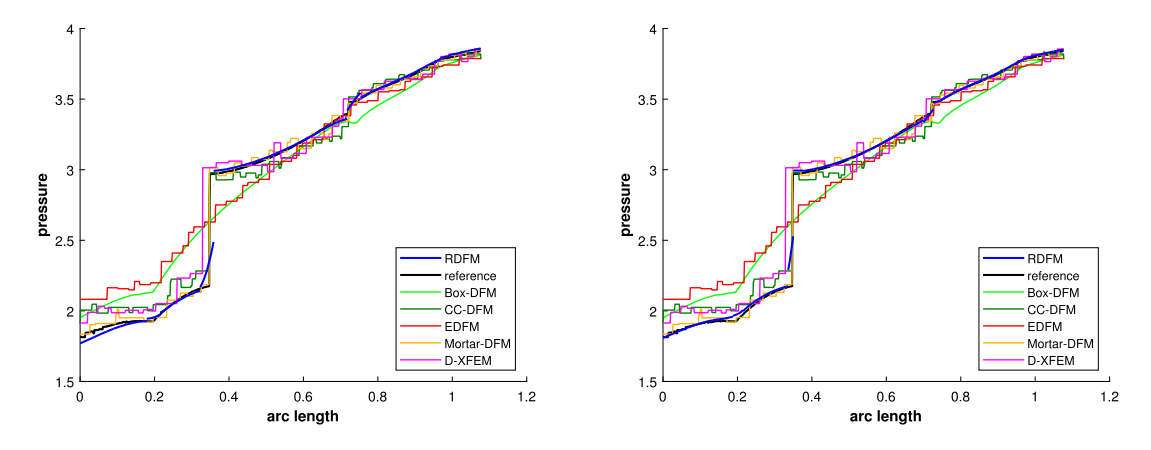
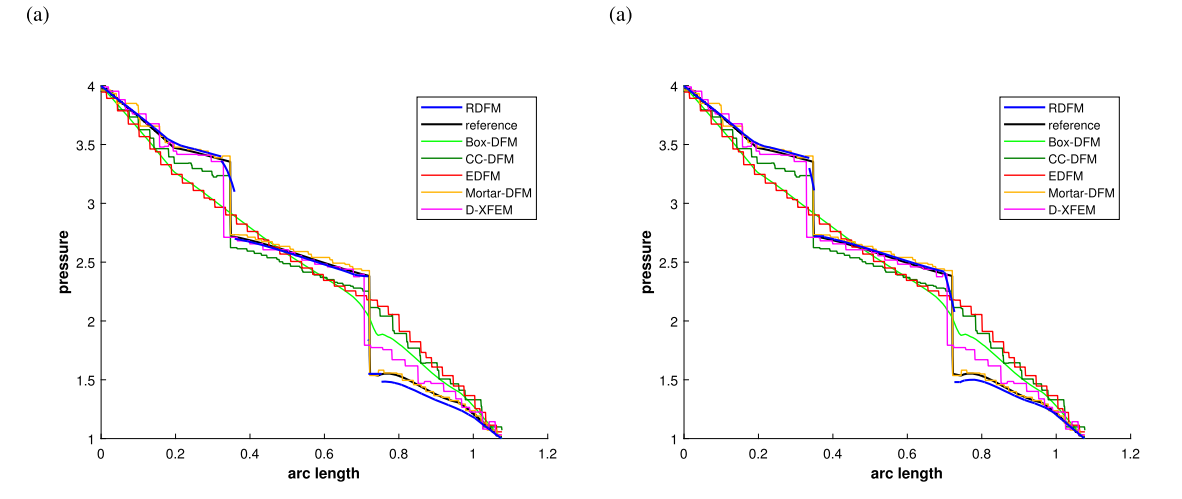


Fig. 16. Simulation results of Example 5.4 on non-conforming meshes.

We first compute the solutions on 30×30 and 40×40 non-conforming uniform rectangular meshes for both cases. Then, we test the model on the conforming triangular meshes with grids data provided by [22], which contains 1332 and 2664 triangles, respectively.

The contour plots of the simulation results on conforming and non-conforming meshes are shown in Fig. 16 and 18, respectively. One can find the contours of the reference solutions in [22] for comparison. We slice the solution along the line (0.0, 0.5) - (1.0, 0.9), and draw the comparison with those of other methods in Fig. 17 and 19.





(c) Pressure along (0.0, 0.5) - (1.0, 0.9) on 30×30 mesh in case (d) Pressure along (0.0, 0.5) - (1.0, 0.9) on 40×40 mesh in case (b)

Fig. 17. Slices of pressure of Example 5.4 on non-conforming meshes.

Table 6Evaluation data of different methods of case (b) of Example 5.4.

method	matrix elements	fracture elements	d.o.f.	mesh	err _m	err_f
Box-DFM	2838 triangles	155	1460	conforming	7.5e-02	7.0e-02
CC-DFM	1407 triangles	103	1510	conforming	5.2e-02	7.3e-02
CC-DFM*	1407 triangles	103	1510	conforming	1.1e-02	2.7e-02
EDFM	1369 rectangles	203	1572	non-conforming	5.8e-02	8.9e-02
Mortar-DFM	1452 triangles	105	3953	conforming	1.3e-02	2.7e-02
D-XFEM	1922 triangles	199	7180	non-conforming	2.2e-02	3.6e-02
RDFM	900 rectangles	167	18000	non-conforming	2.7e-02	5.4e-02
RDFM	1600 rectangles	219	32000	non-conforming	2.3e-02	5.1e-02

We also compare the relative errors on matrix and fractures, and other important aspects of different methods in Table 5 and Table 6 for case (a) and case (b), respectively.

From the tables, we can observe a relatively small matrix error for our methods, but the error on fracture-barrier network is not as small as that on matrix due to the pressure discontinuity on barriers.

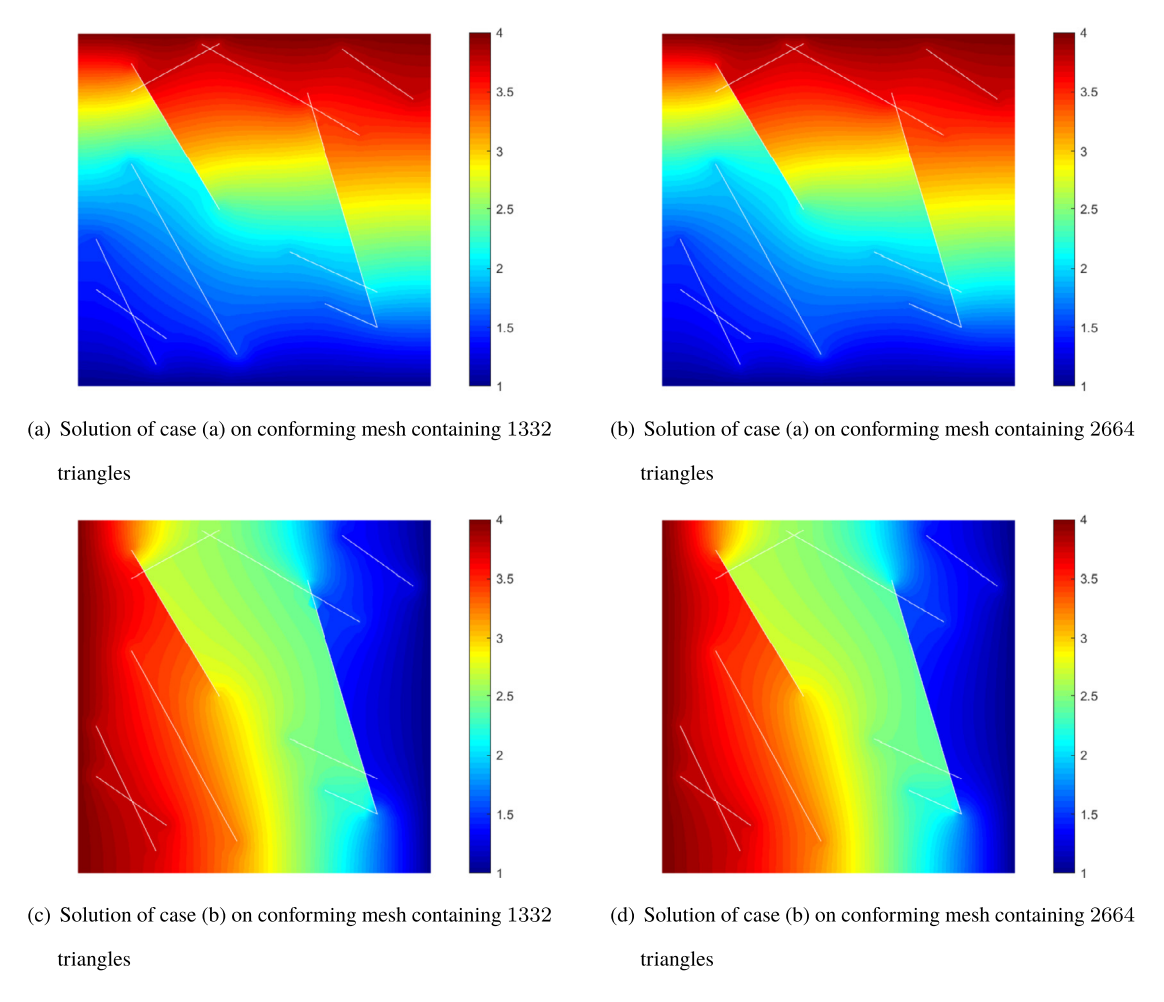


Fig. 18. Simulation results of Example 5.4 on conforming meshes.

6. Applications in contaminant transportation in fractured porous media

In this section, we study the applications of the novel discrete fracture model in contaminant transportation in fractured porous media. The flow field is governed by the equations (3.9), (3.2) and (3.3). The transportation of the contaminant in flow field satisfies the convection-diffusion equation (6.1) with the corresponding boundary conditions (6.2), (6.3) and initial condition (6.4):

$$(\phi c)_t + \nabla \cdot (\mathbf{u}c) - \nabla \cdot (\mathbf{D}\nabla c) = f\tilde{c}, \quad (x,t) \in \Omega \times (0,T]$$

$$(6.1)$$

$$(\boldsymbol{u}\boldsymbol{c} - \boldsymbol{D}\nabla\boldsymbol{c}) \cdot \boldsymbol{n} = c_{\text{in}}\boldsymbol{u} \cdot \boldsymbol{n}, \quad (\boldsymbol{x}, t) \in \Gamma_{\text{in}} \times (0, T]$$

$$(6.2)$$

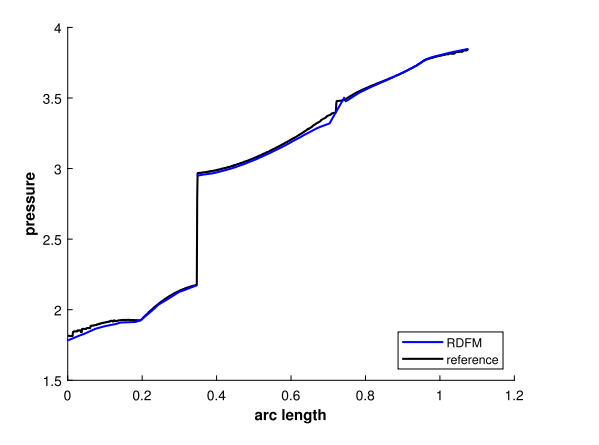
$$(-\mathbf{D}\nabla c) \cdot \mathbf{n} = 0, \quad (x, t) \in \Gamma_{\text{out}} \times (0, T)$$

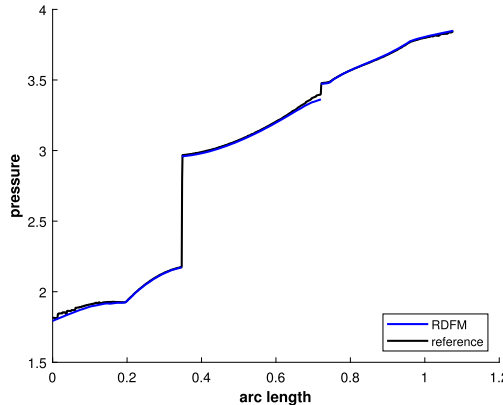
$$(6.3)$$

$$c(x,0) = c_0(x), \quad x \in \Omega, \tag{6.4}$$

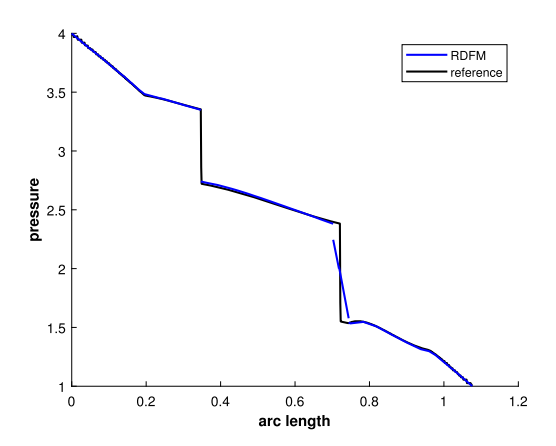
where c is the concentration of the contaminant, ϕ is the porosity of porous media, \boldsymbol{u} is the Darcy's velocity of the flow field, \boldsymbol{D} is the diffusion coefficient of the contaminant, f is the source term, $\tilde{c}=c$ if f<0 and $\tilde{c}=c_{\text{inject}}$ if f>0, Γ_{in} is the inflow boundary and Γ_{out} is the outflow boundary, c_{in} is the concentration of the contaminant on the inflow boundary, c_0 is the initial concentration of the contaminant.

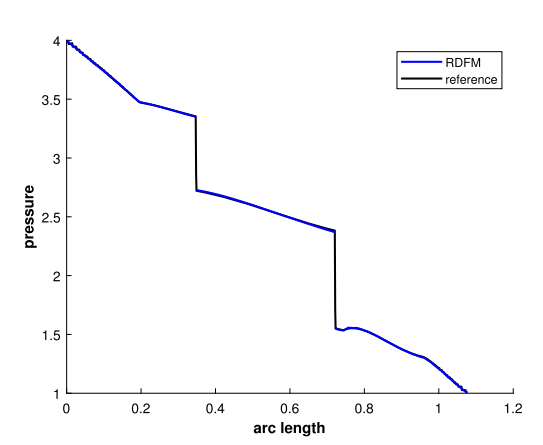
Problem (6.1)-(6.4) is discretized by the interior penalty discontinuous Galerkin (IPDG) method in space. The semidiscrete formulation is given as follows:





(a) Pressure along (0.0, 0.5) - (1.0, 0.9) on conforming mesh containing 1332 triangles in case (a) taining 2664 triangles in case (a)





(c) Pressure along (0.0, 0.5) - (1.0, 0.9) on conforming mesh containing 1332 triangles in case (b) taining 2664 triangles in case (b)

Fig. 19. Slices of pressure of Example 5.4 on conforming meshes.

Find $c \in V_h$, s.t. $\forall v \in V_h$,

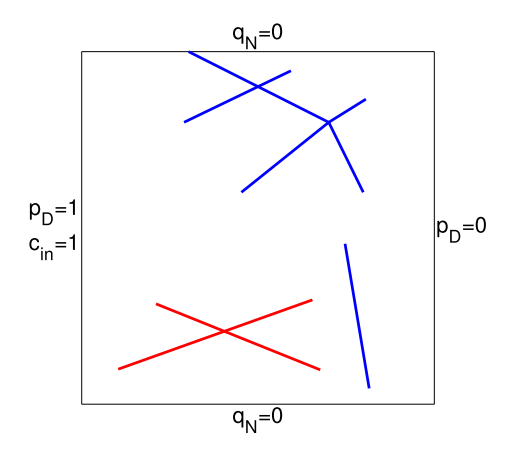
$$(\phi c_{t}, v) = (\boldsymbol{u}c - \boldsymbol{D}\nabla c, \nabla v) - \int_{\Gamma_{0}} \hat{\boldsymbol{u}c}[v] ds - \int_{\Gamma_{\text{in}}} \boldsymbol{u}c_{\text{in}}[v] ds - \int_{\Gamma_{\text{out}}} \boldsymbol{u}c[v] ds + \int_{\Gamma_{0}} (\{\boldsymbol{D}\nabla c\} \cdot [v] + \{\boldsymbol{D}\nabla v\} \cdot [c] - \tilde{\alpha}[c] \cdot [v]) ds + (f\tilde{c}, v),$$

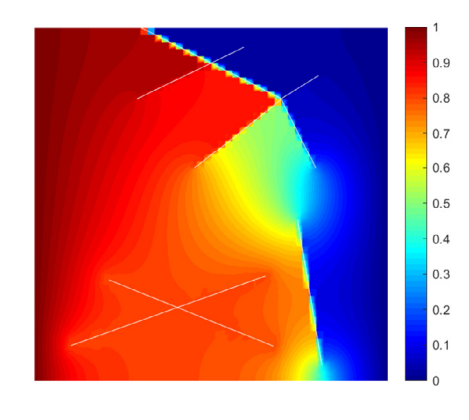
$$(6.5)$$

where $\tilde{\alpha} = O(\frac{1}{|e|})$ is the parameter of the diffusion penalty term and $\hat{uc}|_e = \{uc\} + \tilde{\beta}[c]$ is the Lax-Friedrichs flux on the cell interfaces e.

There are many choices for the time discretization. For simplicity, we use the forward Euler scheme. In the simulation, we first solve for the flow field u from (4.2), (4.3) and (4.4), then simulate the time evolution of the concentration of contaminate in the flow field by computing (6.5). An example is given as below.

Example 6.1. In this example, we simulate the contaminant transportation in the porous media containing fracture and barrier networks. The settings of the problem referred an example in [19] but is not exactly the same. The computational domain is the unit square $\Omega = [0, 1] \times [0, 1]$. The permeability of the porous matrix is $k_m = 1$. The porosity of the porous media is $\phi = 0.2$. The porous media contains 2 fractures and 6 barriers, with the uniform thickness $\epsilon = 1 \times 10^{-4}$, and permeability $k_f = 1 \times 10^8$ and $k_\epsilon = 1 \times 10^{-8}$, respectively. The exact coordinates of the fractures and barriers are attached





(a) Domain and boundary conditions

(b) Pressure distribution on 50×50 mesh

Fig. 20. Domain setting and pressure distribution of Example 6.1.

in the appendix B, see Fig. 20(a) for their distribution. For simplicity, the flow is driven by boundary conditions rather than the source term. The left and right boundaries are Dirichlet with pressure $p_D = 1$ and $p_D = 0$, respectively. The top and bottom boundaries are impermeable. Moreover, the left boundary is an inflow boundary with $c_{in} = 1$ and the right boundary is an outflow boundary. The diffusion coefficient is set to be $\mathbf{D} = 0.005 |\mathbf{u}|$.

The computation is conducted on a 50×50 non-conforming uniform rectangular mesh. The contour plot of the pressure is shown in Fig. 20(b). The time evolution of the concentration of contaminant is exhibited in Fig. 21, with different pore volume injected (PVI).

7. Concluding remarks

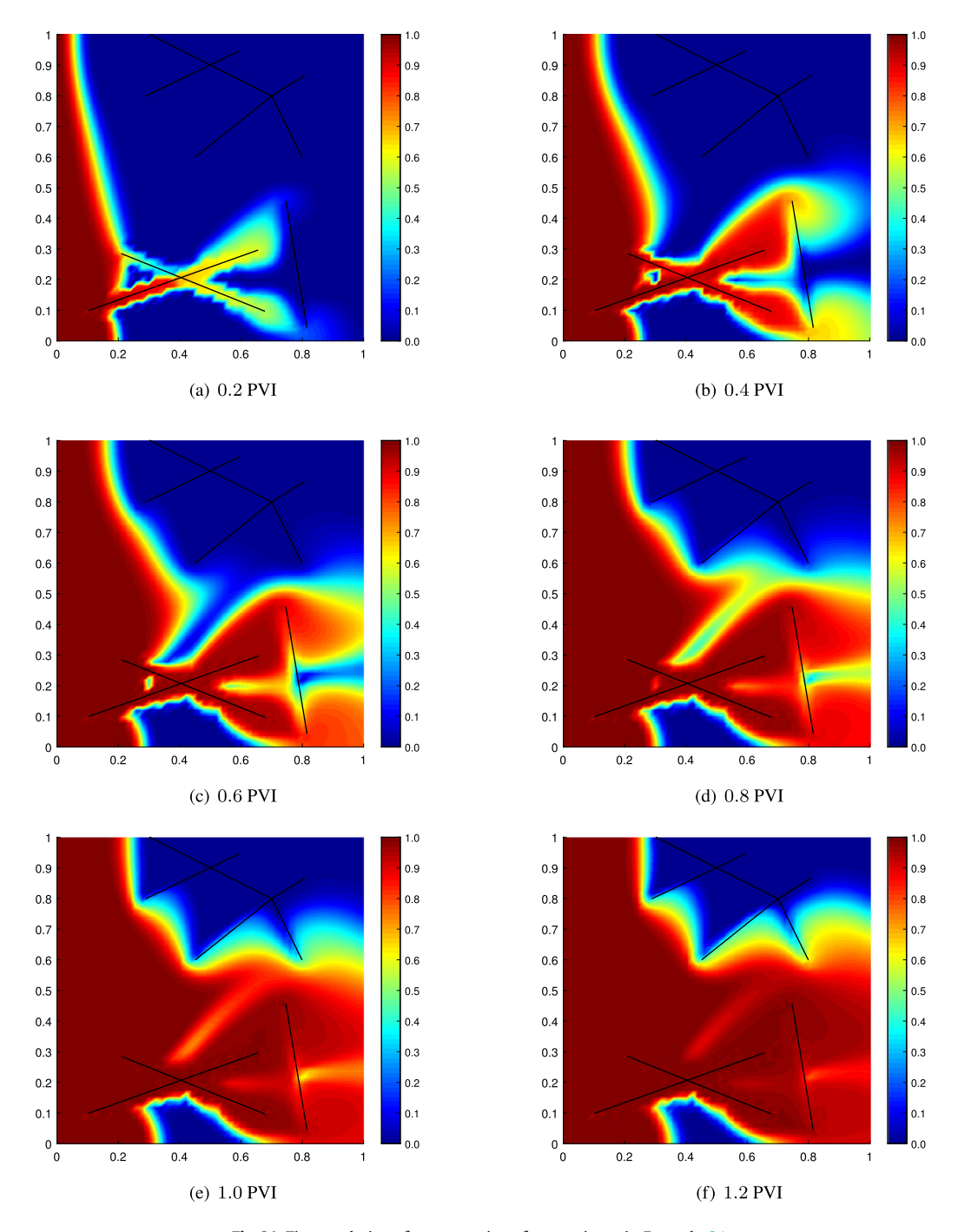
In this paper, we have proposed the hybrid-dimensional Darcy's law and established a novel discrete fracture model by applying the local discontinuous Galerkin method to it. Several numerical experiments show its validity on non-conforming meshes and high accuracy on conforming meshes for porous media containing fracture and barrier networks. Our model doesn't have any restrictions on meshes because it is developed on the PDE level. Moreover, our methods is locally mass conservative thanks to the property of discontinuous Galerkin methods.

Similar to other hybrid-dimensional DFMs and interface models, the physical thickness of fractures are ignored in the model. Therefore, if the thickness of fractures is large, our method has non-negligible model errors. Also, our model can't describe the totally impermeable barriers, i.e. the case $k_{\epsilon}=0$. A major shortcoming of the method is that it has larger degrees of freedom compared with other DFMs based on same triangulation, since the unknowns in LDG scheme include not only pressure but also the Darcy's velocity and gradient of pressure and the solution in each element has independent degrees of freedom.

There are several possible improvements and future works to be done. First, it seems there is no essential difficulties in extending our method to curved fractures and barriers, three dimensional problems, and multi-phase flow in fractured porous media. Therefore it's worthy to explore the performance of the model in these scenarios. Another interesting scenario is the fracture being highly conductive in its tangential direction while low permeable in its normal direction. This kind of 'fracture' can be described by the hybrid-dimensional Darcy's law in principle but doesn't fit the current LDG scheme. We hope to establish an appropriate numerical scheme in future works to simulate this case. In the last, an important direction of our future work is to establish more efficient numerical methods to reduce the large degrees of freedom in the LDG discretization for the PDE model. There have been a series of works [41–43] in this direction, but it is far from fully resolved.

CRediT authorship contribution statement

Ziyao Xu: Conceptualization, Investigation, Methodology, Software, Writing – original draft. **Zhaoqin Huang:** Funding acquisition, Writing – original draft. **Yang Yang:** Conceptualization, Funding acquisition, Investigation, Methodology, Writing – review & editing.



 $\textbf{Fig.\,21.} \ \ \text{Time evolution of concentration of contaminant in Example 6.1.}$

Declaration of competing interest

The authors declare that they have no known competing financial interests or personal relationships that could have appeared to influence the work reported in this paper.

Data availability

Data will be made available on request.

Appendix A. Exact coordinates of fracture networks in Example 5.4

```
FRACTURES:
NUMBER, START_X, START_Y, END_X, END_Y
1, 0.0500 0.4160 0.2200 0.0624;
2. 0.0500 0.2750 0.2500 0.1350;
3, 0.1500 0.6300 0.4500 0.0900;
4, 0.7000 0.2350 0.8500 0.1675;
5, 0.6000 0.3800 0.8500 0.2675;
6, 0.3500 0.9714 0.8000 0.7143;
7, 0.7500 0.9574 0.9500 0.8155;
8, 0.1500 0.8363 0.4000 0.9727;
BARRIERS
NUMBER, START_X, START_Y, END_X, END_Y
1, 0.1500 0.9167 0.4000 0.5000;
2, 0.6500 0.8333 0.8500 0.1667;
```

Appendix B. Exact coordinates of fracture networks in Example 6.1

```
FRACTURES:
NUMBER, START_X, START_Y, END_X, END_Y
1, 0.2107 0.2846 0.6765 0.0974;
2. 0.1035 0.0993 0.6543 0.2959;
BARRIERS
NUMBER, START_X, START_Y, END_X, END_Y
1, 0.3031 1.0000 0.7006 0.7996;
2, 0.7006 0.7996 0.7985 0.6011;
3, 0.2902 0.7996 0.5933 0.9457;
4, 0.4529 0.6011 0.7006 0.7996;
5, 0.7006 0.7996 0.8059 0.8652;
6, 0.7468 0.4551 0.8152 0.0449;
```

Appendix C. A concrete example showing the mass transfer between fractures and matrix in the model

Our model has the intrinsic mechanism of handling mass transfer between fractures and matrix, which can be demonstrated by a concrete example given below.

We have the exact solution $p(x, y) = \sin(x)e^{|y|}$ to the model

$$\boldsymbol{u} = - \begin{pmatrix} \mathbf{I} + 2\delta(y) \begin{bmatrix} 1 & 0 \\ 0 & 0 \end{bmatrix} \end{pmatrix} \nabla p, \quad \nabla \cdot \boldsymbol{u} = 0,$$

which is obtained by taking $\theta = 0$ in the case (a) of the Example 5.1. The equation models a single conductive fracture along y = 0 with conductivity $\epsilon k_f = 2$ in an infinite domain (or a bounded domain if a compatible boundary condition of the solution is given).

It's easy to compute that the Darcy's velocity of the flow in the domain is

$$\mathbf{u} = (u_1, u_2)^T = -\left((1 + 2\delta(y))\cos(x)e^{|y|}, \operatorname{sign}(y)\sin(x)e^{|y|}\right)^T, \quad (x, y) \in \mathbb{R}^2$$

Therefore, the mass flow into the fracture y=0 between x=0 and $x=\frac{\pi}{2}$ from the below and above of porous matrix are

$$\int_{0}^{\frac{\pi}{2}} u_{2}(x, 0^{-}) dx = \int_{0}^{\frac{\pi}{2}} \sin(x) dx = 1,$$

and

$$\int_{0}^{\frac{\pi}{2}} -u_{2}(x, 0^{+}) dx = \int_{0}^{\frac{\pi}{2}} \sin(x) dx = 1,$$

respectively. This result clearly shows the mass transfer between matrix and fractures in our model.

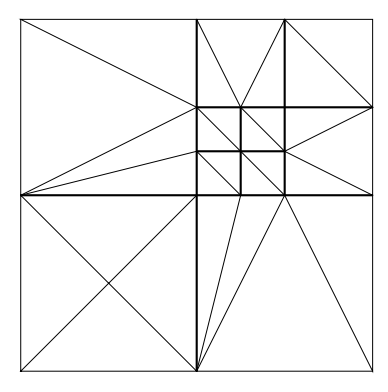


Fig. 22. Triangulation of the domain (28 elements) of Example 5.3.

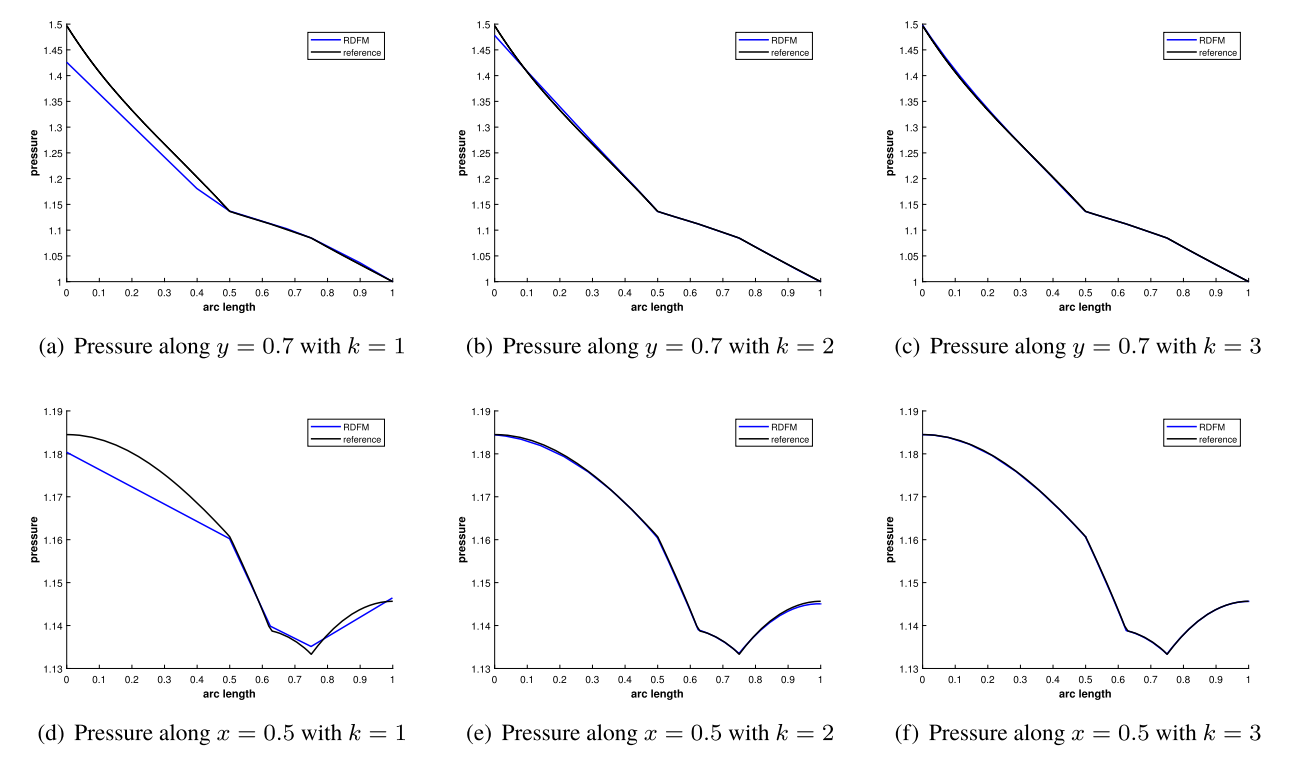
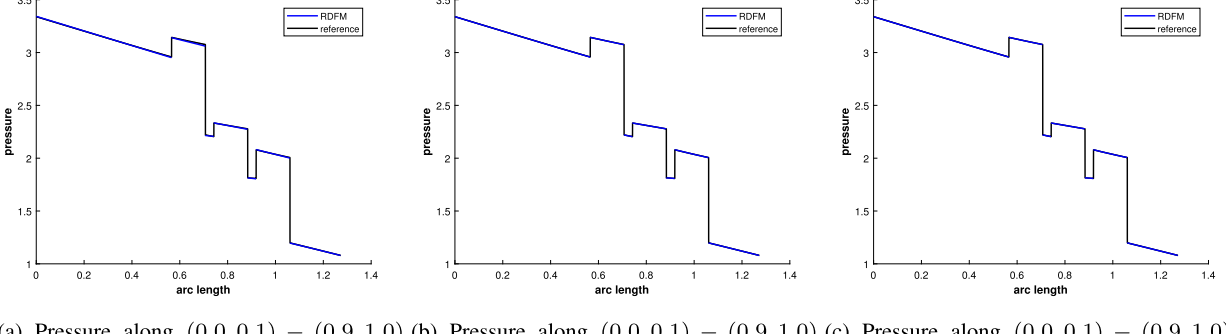


Fig. 23. Slices of pressure in case (a) of Example 5.3 on the coarse conforming mesh 22.



(a) Pressure along (0.0,0.1)-(0.9,1.0) (b) Pressure along (0.0,0.1)-(0.9,1.0) (c) Pressure along (0.0,0.1)-(0.9,1.0) with k=1 with k=3

Fig. 24. Slices of pressure in case (b) of Example 5.3 on the coarse conforming mesh 22.

Appendix D. A cursory investigation on high order LDG discretization for the model on conforming meshes

As shown in the Example 5.1, the solution converges with optimal order of accuracy on conforming meshes. In this section, we carry out a cursory investigation on high order LDG method for the model on conforming meshes.

We apply the LDG scheme with order k = 1, 2, 3 on a coarse conforming triangular mesh containing 28 cells for the Example 5.3. The mesh visualization is given in Fig. 22. We plot the slices of pressure along the line y = 0.7 and x = 0.5 for the case (a) in Fig. 23, and along the line (0.0, 0.1) - (0.9, 1.0) for the case (b) in Fig. 24, from which we can observe an excellent agreement with the exact solution as k increases.

References

- [1] B. Berkowitz, Characterizing flow and transport in fractured geological media: a review, Adv. Water Resour. 25 (8-12) (2002) 861-884.
- [2] J.S. Caine, J.P. Evans, C.B. Forster, Fault zone architecture and permeability structure, Geology 24 (11) (1996) 1025-1028.
- [3] A. Fumagalli, L. Pasquale, S. Zonca, S. Micheletti, An upscaling procedure for fractured reservoirs with embedded grids, Water Resour. Res. 52 (8) (2016) 6506–6525.
- [4] S. Granet, P. Fabrie, P. Lemonnier, M. Quintard, A two-phase flow simulation of a fractured reservoir using a new fissure element method, J. Pet. Sci. Eng. 32 (1) (2001) 35–52.
- [5] H. Hoteit, A. Firoozabadi, An efficient numerical model for incompressible two-phase flow in fractured media, Adv. Water Resour. 31 (6) (2008) 891–905.
- [6] Z. Huang, X. Yan, J. Yao, A two-phase flow simulation of discrete-fractured media using mimetic finite difference method, Commun. Comput. Phys. 16 (3) (2014) 799–816.
- [7] J. Jiang, R.M. Younis, An improved projection-based embedded discrete fracture model (pEDFM) for multiphase flow in fractured reservoirs, Adv. Water Resour. 109 (2017) 267–289.
- [8] M. Karimi-Fard, L. Durlofsky, K. Aziz, An efficient discrete fracture model applicable for general purpose reservoir simulators, Paper SPE 79699 presented at the SPE Reservoir Simulation Symposium. Soc. Pet. Eng., Houston, Tex 2003.
- [9] M. Karimi-Fard, A. Firoozabadi, Numerical simulation of water injection in 2D fractured media using discrete-fracture model, in: SPE Annual Technical Conference and Exhibition, Society of Petroleum Engineers, 2001, January.
- [10] J.G. Kim, M.D. Deo, Finite element, discrete-fracture model for multiphase flow in porous media, AlChE J. 46 (6) (2000) 1120-1130.
- [11] S.H. Lee, M.F. Lough, C.L. Jensen, Hierarchical modeling of flow in naturally fractured formations with multiple length scales, Water Resour. Res. 37 (3) (2001) 443–455.
- [12] L. Li, S.H. Lee, Efficient field-scale simulation of black oil in a naturally fractured reservoir through discrete fracture networks and homogenized media, SPE Reserv. Eval. Eng. 11 (04) (2008) 750–758.
- [13] L. Liu, Z. Huang, J. Yao, Y. Di, Y.S. Wu, An efficient hybrid model for 3D complex fractured vuggy reservoir simulation, SPE J. 25 (2) (2020) 907–924.
- [14] V. Martin, J. Jaffré, J.E. Roberts, Modeling fractures and barriers as interfaces for flow in porous media, SIAM J. Sci. Comput. 26 (5) (2005) 1667–1691.
- [15] A. Moinfar, A. Varavei, K. Sepehrnoori, R.T. Johns, Development of an efficient embedded discrete fracture model for 3D compositional reservoir simulation in fractured reservoirs, SPE J. 19 (02) (2014) 289–303.
- [16] A. Obeysekara, Q. Lei, P. Salinas, D. Pavlidis, J. Xiang, J.P. Latham, C.C. Pain, Modelling stress-dependent single and multi-phase flows in fractured porous media based on an immersed-body method with mesh adaptivity, Comput. Geotech. 103 (2018) 229–241.
- [17] O. Olorode, B. Wang, H.U. Rashid, Three-dimensional projection-based embedded discrete-fracture model for compositional simulation of fractured reservoirs, SPE J. 25 (4) (2020) 2143–2161.
- [18] P. Panfili, A. Cominelli, Simulation of miscible gas injection in a fractured carbonate reservoir using an embedded discrete fracture model, in: Abu Dhabi International Petroleum Exhibition and Conference, Society of Petroleum Engineers, 2014, November.
- [19] M. Tene, S.B. Bosma, M.S. Al Kobaisi, H. Hajibeygi, Projection-based embedded discrete fracture model (pEDFM), Adv. Water Resour. 105 (2017) 205–216
- [20] Y. Xu, K. Sepehrnoori, Development of an embedded discrete fracture model for field-scale reservoir simulation with complex corner-point grids, SPE I. 24 (04) (2019) 1–552.
- [21] Z. Xu, Y. Yang, The hybrid dimensional representation of permeability tensor: a reinterpretation of the discrete fracture model and its extension on nonconforming meshes, J. Comput. Phys. 415 (2020) 109523.
- [22] B. Flemisch, I. Berre, W. Boon, A. Fumagalli, N. Schwenck, A. Scotti, I. Stefansson, A. Tatomir, Benchmarks for single-phase flow in fractured porous media, Adv. Water Resour. 111 (2018) 239–258.
- [23] L.H. Odsæter, T. Kvamsdal, M.G. Larson, A simple embedded discrete fracture–matrix model for a coupled flow and transport problem in porous media, Comput. Methods Appl. Mech. Eng. 343 (2019) 572–601.
- [24] S. Geiger, M. Dentz, I. Neuweiler, A novel multi-rate dual-porosity model for improved simulation of fractured and multi-porosity reservoirs, in: SPE Reservoir Characterisation and Simulation Conference and Exhibition, Society of Petroleum Engineers, 2011, January.
- [25] N. Schwenck, An XFEM-Based Model for Fluid Flow in Fractured Porous Media, 2015.
- [26] M. Köppel, V. Martin, J. Jaffré, J.E. Roberts, A Lagrange multiplier method for a discrete fracture model for flow in porous media, Comput. Geosci. 23 (2) (2019) 239–253.
- [27] T.H. Sandve, I. Berre, J.M. Nordbotten, An efficient multi-point flux approximation method for discrete fracture-matrix simulations, J. Comput. Phys. 231 (9) (2012) 3784–3800.
- [28] R. Ahmed, M.G. Edwards, S. Lamine, B.A. Huisman, M. Pal, Control-volume distributed multi-point flux approximation coupled with a lower-dimensional fracture model, J. Comput. Phys. 284 (2015) 462–489.
- [29] D. Gläser, R. Helmig, B. Flemisch, H. Class, A discrete fracture model for two-phase flow in fractured porous media, Adv. Water Resour. 110 (2017) 335–348.
- [30] N. Zhang, J. Yao, Z. Huang, Y. Wang, Accurate multiscale finite element method for numerical simulation of two-phase flow in fractured media using discrete-fracture model, J. Comput. Phys. 242 (2013) 420–438.
- [31] H. Hoteit, A. Firoozabadi, Numerical simulation of gas injection in discrete-fractured reservoirs without transfer functions using the discontinuous Galerkin and mixed methods, SPE J. (Sept 2006) 341–352.
- [32] J. Moortgat, A. Firoozabadi, Three-phase compositional modeling with capillarity in heterogeneous and fractured media, in: SPE Annual Technical Conference and Exhibition, Society of Petroleum Engineers, 2012, January.
- [33] A. Zidane, A. Firoozabadi, An efficient numerical model for multicomponent compressible flow in fractured porous media, Adv. Water Resour. 74 (2014) 127–147.

- [34] A. Zidane, A. Firoozabadi, Reservoir simulation of fractured media in compressible single-phase flow in 2D, 2.5 D and 3D unstructured gridding, Adv. Water Resour. 121 (2018) 68–96.
- [35] B. Rivière, Discontinuous Galerkin Methods for Solving Elliptic and Parabolic Equations: Theory and Implementation, Society for Industrial and Applied Mathematics, 2008.
- [36] B. Cockburn, C.W. Shu, The local discontinuous Galerkin method for time-dependent convection-diffusion systems, SIAM J. Numer. Anal. 35 (6) (1998) 2440–2463.
- [37] G. Chavent, J. Jaffré, Mathematical Models and Finite Elements for Reservoir Simulation: Single Phase, Multiphase and Multicomponent Flows Through Porous Media, Elsevier, 1986.
- [38] H. Hoteit, P. Ackerer, R. Mosé, Nuclear waste disposal simulations: couplex test cases, Comput. Geosci. 8 (2) (2004) 99-124.
- [39] H. Hoteit, A. Firoozabadi, Multicomponent fluid flow by discontinuous Galerkin and mixed methods in unfractured and fractured media, Water Resour. Res. 41 (11) (2005).
- [40] https://git.iws.uni-stuttgart.de/benchmarks/fracture-flow.
- [41] H. Guo, W. Feng, Z. Xu, Y. Yang, Conservative numerical methods for the reinterpreted discrete fracture model on non-conforming meshes and their applications in contaminant transportation in fractured porous media, Adv. Water Resour. 153 (2021) 103951.
- [42] G. Fu, Y. Yang, A hybrid-mixed finite element method for single-phase Darcy flow in fractured porous media, Adv. Water Resour. 161 (2022) 104129.
- [43] G. Fu, Y. Yang, A hybridizable discontinuous Galerkin method on unfitted meshes for single-phase Darcy flow in fractured porous media, arXiv preprint, arXiv:2209.05445, 2022.